



UNIVERSITY OF LEEDS

Transfer Report

Ryan Brook

**The University of Leeds
School of Chemistry**

July 2023

Abstract

There have been numerous methods developed to solve the Time-dependent Schrodinger equation in a computationally efficient manner. New methods or extensions/improvements to existing methods are often tested with the spin-boson model. While numerous methods have accurately calculated results for certain parameters of the model, there are several regimes that present challenges. The other main issue is that the issues struggle with systems with large modes and degrees of freedom. The multiconfigurational Ehrenfest method has great scaling potential and with the introduction of the cloning procedure, may be capable of converging to the correct result across all regimes of the spin boson model.

Contents

1	Background	1
1.1	A brief history	1
1.2	Development of MCE	4
1.3	The spin boson models and methods to solve it	12
2	Current work	20
3	Future work	40
4	References	42

List of Figures

2.3 Population difference calculated by MCEv1 at zero-temperature. Symmetrical well case with parameters $\omega_c/\delta = 10$, $\alpha_k = 1.5$, $\epsilon=0$, $\beta\delta=1000$ (a suitable estimation of infinity is required). All runs consisted on $N_{rpts} = 128$ repeats and $M = 200$ bath modes and $N_{bfs} = 50$. The number of cloning events were varied for each run.	22
2.4 Population difference for a symmetrical well case with exponential cutoff with the same parameters as Figure 2.2. Cloning once (orange) occurred at timestep 1000, and the cloning thrice (green had cloning events at timesteps 500,1000,1500). The propagation with 3 cloning events matches perfectly the original converged MCEv1 result(blue).	25
2.5 Population difference after cloning for the symmetrical well case shown in Figure 2.2. The number in the legend denotes the timestep(s) for the cloning event(s) for each propagation.	26
2.6 The evolution of cross terms throughout a propagation with the same parameters as Figure 2.2 with a cloning event at timestep 1000 out of a total of 2000 timestep.	27
2.7 The evolution of cross terms throughout a propagation with the same parameters as Figure 2.2 with a cloning event at timesteps 750 out of a total of 2000.	27
2.8 The evolution of cross terms throughout a propagation with the same parameters as Figure 2.2 with cloning events at timesteps 750 and 1500 out of a total of 2000.	28
2.9 The normalisation re-scale factor shown for each of the different propagations shown in figure 2.5.	29
2.10 Relocalisation case with parameters $\omega_c = 10$, $\beta = 5000$ (as an estimation of infinity), $\alpha_k = 1.5$. The propagations were run with $N_{bfs} = 200$ and $M=200$ but with only 16 repeats. The number in the legend denotes the timestep of the cloning event	30
2.11 The evolution of cross terms throughout a propagation with the same parameters as Figure 2.10 with a cloning event at timestep 1000 out of a total of 2000.	30
2.12 Population difference of case 2 with and without the inclusion of cross-terms after a cloning event at timestep 1000 of 2000.	31
2.13 The evolution of cross terms throughout a propagation with the same parameters as Figure 2.10 with a cloning event at timestep 30 out of a total of 2000.	32

2.14 The evolution of cross terms throughout a propagation with the same parameters as Figure 2.10 with a cloning event at timestep 40 out of a total of 2000.	32
2.15 Population difference of case 2 with and without the inclusion of cross-terms after a cloning event at timestep 30 of 2000.	33
2.16 Population difference of case 2 with and without the inclusion of cross-terms after a cloning event at timestep 30 of 2000.	33
2.17 Incoherent relaxation case with parameters $\omega_c = 7.5$, $\alpha_k = 0.6$, $\beta = 5$ and $\epsilon = 0$. The propagation was ran with 200 basis functions and 200 bath modes. The number in the legend dentotes the timestep of cloning.	34
2.18 The evolution of cross terms throughout a propagation with the same parameters as Figure 2.17 with a cloning event at timestep 100 out of a total of 2000.	35
2.19 The evolution of cross terms throughout a propagation with the same parameters as Figure 2.17 with a cloning event at timestep 100 out of a total of 2000.	35
2.20 The evolution of cross terms throughout a propagation with the same parameters as Figure 2.17 with a cloning event at timestep 1500 out of a total of 2000.	36
2.21 Population difference of case 3 with and without the inclusion of cross-terms after a cloning event at timestep 1500 of 2000.	37
2.22 Figure 1 copied from reference 101 to serve as a benchmark. The coupling strength α is given by the legend of each graph. Graph (a), (b), (c) have the characteristic frequencies $\omega_c = 10/20/40$ respectively at 0 temperature.	38
2.23 Cases from figure 2.23 b run with parameters $\omega_c = 20$, $\beta = 5000$ (to estimate infinity) and α_k ranging from 0.05 to 0.5. Propagation were carried out at $N_{bfs} = 200$, $M = 500$ and with 64 repeats.	38
2.24 Cases from figure 2.23 b run with parameters $\omega_c = 20$, $\beta = 5000$ (to estimate infinity) and α_k ranging from 0.05 to 0.5. Propagation were carried out at $N_{bfs} = 200$, $M = 500$ and with 64 repeats.	39

List of Tables

Chapter 1

Background

Quantum mechanics has a strong reputation for being a demanding field of study. Beyond demanding the understanding of complex and sometimes non-intuitive topics, quantum mechanics is also famous for the exigent need of computational power. Since its inception, quantum mechanics has suffered from the infamous 'curse of dimensionality'(1, 2). Accounting for additional degrees of freedom in a quantum Hamiltonian leads to an exponential increase in the computational power required to retrieve the exact solution of the Schrodinger equation. This leads to systems of interest, which are relatively large on a quantum scale, being unapproachable objects of study due to the computational power needed being inaccessible or unfeasible. Therefore understanding of quantum mechanics does not evolve in a purely theoretical manner, but rather in tandem with the advent of larger computational power or creation of a method that has a more efficient use of existing computational power.

1.1 A brief history

In 1966, Secrest and Johnson published a paper in which they showed they were capable of producing exact quantum mechanical transition probabilities for atom-diatom collisions(3). These results then became the benchmarks for many approximations, one of which was Miller's approach of rewriting the classical S-matrix(4, 5),which can be considered to be the first method of the Initial-Value Representation(IVR) approach. As with most methods of the time, this was a semiclassical approach, aiming to balance the exponential scaling problem with the accuracy of results by relying on classical mechanics and trajectories to greatly reduce computational

demands while capturing quantum mechanical effects such as tunnelling. Miller's approach uses the Wentzel–Kramers–Brillouin (WKB) approximation to calculate the phase shift of the quantum mechanical cross section of collision. This allows the production of the scattering matrix whose scattering amplitudes contain purely classical terms, yet can describe quantum mechanical effects due to mathematical tricks such as superposition. Miller presents the quantum mechanical equations with the substitution for the S-matrix and proceeds to show how the classical S-matrix can be found through purely classical dynamics before being inserted into the quantum mechanical equations.

The IVR class of semiclassical methods has been expanded and developed significantly since Miller's first publication on the classical S-matrix(6, 7), and various methods have now been applied to many problems(8-16). The name comes from the solution to a problem that semiclassical methods face, that is generating trajectories that are capable of satisfying the boundary problems of the system, i.e. finding trajectories with varying momentum but have initial and final conditions concurrent with the movement of the system is a computationally expensive task. IVR's solution to this problem is to rewrite the integration over both initial and final coordinates to an average over just the initial conditions(6). This has the useful consequence of changing the difficult 'root search' problem (to which efficient algorithms for solving are still being developed 50 years after Miller published(17)) to a simple propagation of classical trajectories, making IVR methods notably analogous to classical molecular dynamics, while still maintaining several quantum advantages.

While all IVR methods share this strength, they also share innate weaknesses such as tunneling being a quantum effect that is difficult to capture(4, 18, 19) (a significant problem for several early methods, though schemes and updated methods have been developed(20)), and that they suffer from the dynamic sign problems that results from summing over multiple path integrals (another area still presently being researched(21, 22)). In the present day, advancements from several different research groups have led to many different forms of IVR methods in order to be applied to more complex systems. One such example of this is mixed quantum classical initial value representation (MQC-IVR)(23, 24) which has been developed to encapsulate the semiclassical ideal by reproducing the results of two separate methods, the more expensive Herman–Kluk IVR that excels at capturing quantum effects at the quantum limit(25-27), and the more scale-able linearised IVR which has been successfully applied to large systems but is

constrained to a short time-frame(28-33).

One of the main advantages of linearised IVR is the reduction of computational time by making additional approximations that bypass the sign problem, something that more expensive but accurate methods such as the aforementioned Herman-Kluk IVR encounters by having to converge heavily oscillatory integrals. MQC-IVR takes a similar approach to solving this problem. It begins by taking the Double Herman-Kluk approximation of the time-evolution operators in real time correlation functions, which then undergoes a transformation of variables and application of modified Fillinov filtration. Fillinov filtration involves the introduction of an additional oscillating term that serves to, at least in the relevant necessary regions, cancels out the oscillations of the original integrand reducing the severity of the sign problem. The modified fillinov filtration is a more advanced application where the extent of the scheme is controlled via the elements of a matrix with dimensions $2N \times 2N$ where N is the size of smaller matrices, c_q and c_p ,

$$\begin{pmatrix} c_q & 0 \\ 0 & c_p \end{pmatrix} \quad (1.1)$$

Here the smaller internal matrices represent the displacement of a given degree of freedom in terms of position and momentum respectively whereas the 0s represent an $N \times N$ null matrix. Adjustment allows for control of the extent to which any given degree of freedom is treated quantumly. Therefore after identifying the most relevant modes of a system it is possible to set these matrices in a state that allows for dampening of the problematic oscillations that result in the dynamic sign problem without losing accuracy. As previously stated, MCQ-IVR is a flexible method as setting the internal matrices to 0 yields the Herman-Kluk IVR, allowing for the full accuracy provided by the expensive methods but as the parameters inside the internal matrices increase, the MCQ-IVR then resembles methods that function at the classical limit of the semiclassical methods.

Another group of methods is based upon equally seminal work, the concept of Gaussian wave packets, published by Heller(34). In this work, Heller showed that the wavefunction of a particle in a harmonic potential can be represented by these Gaussian wave packets. The time

dependence of the wavefunction can then be recovered by the spreading of the wave packet, as well as change in its position and momentum. Calculating several different trajectories of these Gaussian wave packets allows for a more complete sampling of the systems dynamics and can therefore be used to construct an S-matrix allowing application of the method to scattering problems. Gaussian wave packets have several immediate advantages, as individual trajectories are no longer in violation of the uncertainty principle as with previous classical trajectories and a Gaussian wave packet is actually the exact wave function of a harmonic oscillator. When Gaussian wave packets are applied to non-harmonic potentials, it is often more efficient to derive the relevant equations of motion variationally, leading to Variational Gaussians(35, 36). In the best ideal cases, Gaussian wave packets (i.e. the number of parameters required to describe them) scale linearly with the dimensionality of the system presenting a perfect candidate for producing qualitative information about large systems, and an extension aptly extended thawed Gaussian approximation (ETGA) was in fact recently used to accurately generate spectra of polyatomic systems such as benzene(37).

If instead the Gaussian wave packets are not allowed to spread and their width kept constant, the Frozen Gaussian approximation (FGA) can be derived(38). Within this approximation, it is possible to transform both the initial and final wavefunction into an exact superposition of Gaussian wave packets. The FGA was shown capable of reproducing Frank-Condon spectra for different potentials, namely Barbanis and Hénon-Heiles, before being used to solve scattering problems(39).

1.2 Development of MCE

The method of Coupled Coherent States(CCS) by Shalashilin and Child was an exact quantum mechanical method for solving the Schrodinger equation that was first published in 2000(49). This method borrows a lot of common ideas from semiclassical methods, utilising frozen Gaussian Coherent states guided by certain trajectories that are ascertained from the Hamiltonian averaged over the wavefunction, but also boasts multiple advantages. Firstly, CCS allows for the quantum amplitudes calculated to be exact with the only approximation being that the basis set is large enough. When compared to other methods that utilise variationally derived trajectories, CCS trajectories are much easier to calculate and propagate, and they're significantly more stable, not having to face numerical instability of certain regions(50). Additionally,

as the overlap between different coherent states of the basis set constitutes the Hamiltonian matrix, and this overlap can be shown to be small for coherent states that are both close and far, the Hamiltonian can be said to be ‘sparse’ providing the benefit of being easy to calculate and manipulate. The need to inverse a complicated singular matrix, a problem faced by several methods, is completely avoided by CCS. CCS was later shown to be applicable to higher dimensional systems(51-53) and capable of producing accurate spectroscopy(54, 55).

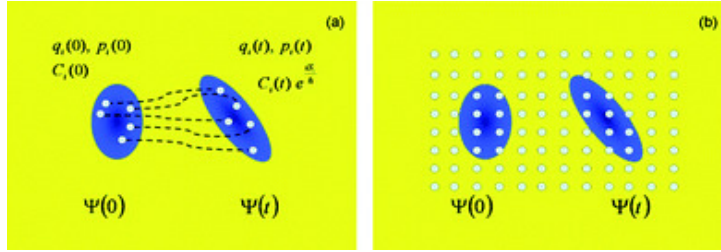


Figure 1.1: Graphic showing the advantage of a moving trajectory guided basis set. Significantly fewer basis functions are required to represent the whole wavefunction than with the traditional rigorous grid method. Copied from reference 1.

A few years later in 2009, Shalashilin published the Multiconfigurational Ehrenfest method version 1(MCEv1)(56). The method also uses a trajectory guided coherent state basis set but applied to a system with multiple different potential energy surfaces. The coherent states are now guided by Ehrenfest trajectories which are determined by the potential energy surfaces. The MCE method is well suited for simulating small timeframe quantum processes, such as those found in photochemistry, an interesting field of study with a wide range of areas from photoprotection of DNA(60-62) to photon pumps such as bacteriorhodopsin (63-67).

The method was first applied to the spin boson model, a two-level open quantum system, while showing improvements on computation time compared to the benchmark, Multiconfigurational time dependent Hartree (MCTDH) (57, 58). MCEv1 uses an ansatz of the total wavefunction where the different electronic states are weighted by quantum amplitudes, with the nuclear part of the wavefunction being represented by a bath of frozen Gaussian Coherent states. The MCEv1 ansatz is said to be single set, meaning that all the different electronic states (within a basis function) share the same coherent states. The equations for the method below are presented for 2 electronic states but can be generalised to include more,

$$|\Psi(t)\rangle = \sum_{k=1,N} (a_k^{(1)}|1\rangle + a_k^{(2)}|2\rangle)|z_k(t)\rangle \quad (1.2)$$

the quantum amplitudes are derived by applying the variational principle and are usually written in the form of the classical action multiplied by a pre-exponential factor,

$$a_k^{(r)} = d_k^{(r)} e^{(iS_k^{(r)})} \quad (1.3)$$

$$\dot{d}_1 = -iH_{12}d_2e^{(i(S_2-S_1))} \quad (1.4)$$

$$\dot{d}_2 = -iH_{21}d_1e^{(i(S_1-S_2))} \quad (1.5)$$

Applying the same idea of the variational principle to the coherent states leads to the equation,

$$i\dot{z}_k = \frac{\partial H^{Ehr}}{\partial z_k^*} \quad (1.6)$$

and the trajectories are guided by the normalised Ehrenfest force of the system,

$$F_n = \frac{\sum_{IJ} a_{nI}^* a_{nJ} \frac{\partial V_{nInJ}}{\partial R}}{\sum_{IJ} a_{nI}^* a_{nJ}} \quad (1.7)$$

where H^{Ehr} is the Ehrenfest Hamiltonian, found by averaging the total quantum Hamiltonian over the total system wavefunction. As the different basis functions of MCEv1 are coupled with each other, the introduction of ab initio 'on the fly' dynamics is more difficult than for other

methods. However this inter-coupling also poses several advantages, as MCEv1 does not require an exponential increase in basis functions in order to model larger systems, allowing it to scale to systems too large for other methods. The trajectories for MCEv1 also interact through the inter-coupling, and can be described as 'pushing' other trajectories along in phase space, which helps combat one of the big problems of trajectory based methods, which is that with time all trajectories spread out and therefore completely uncouple and stop interacting causing a breakdown in accurate propagation.

Multiconfigurational Ehrenfest version 2 (MCEv2) was published a year later as an improvement to the theory(67), modifying the original ansatz by the inclusion of an additional amplitude weighting each individual basis function,

$$|\Psi(t)\rangle = \sum_{k=1,N} D_k(t)|\psi(t)\rangle = \sum_{k=1,N} D_k(t)(a_k^{(1)}|1\rangle + a_k^{(2)}|2\rangle)|z_k(t)\rangle \quad (1.8)$$

meaning that the amplitudes between each basis function are no longer coupled, meaning that the trajectories are no longer capable of 'pushing' each other and can be described as independent Ehrenfest trajectories as opposed to MCEv1's coupled Ehrenfest trajectories. The fact that the trajectories are uncoupled allows for them to be run individually and in fact before quantum simulation, a great advantage for any method that could be used for ab initio direct dynamics. MCEv2 originally found success in simulating real molecules, using a small basis set of only 250 FG per state to produce accurate absorption spectra of pyrazine, up to the 24 dimensional model, before the method's efficiency was combined with information from electronic structure packages to create an ab initio 'on the fly' direct dynamic method known as Ab Initio Multiple Cloning(AIMC)(68).

MCEv1	MCEv2
$(a_1^{(1)} 1\rangle + a_0^{(1)} 0\rangle) \mathbf{z}^{(1)}(t)\rangle$	$A^{(1)}(a_1^{(1)} 1\rangle + a_0^{(1)} 0\rangle) \mathbf{z}^{(1)}(t)\rangle$
$(a_1^{(2)} 1\rangle + a_0^{(2)} 0\rangle) \mathbf{z}^{(2)}(t)\rangle$	$A^{(2)}(a_1^{(2)} 1\rangle + a_0^{(2)} 0\rangle) \mathbf{z}^{(2)}(t)\rangle$

Figure 1.2: Ansatz for both MCEv1 and MCEv2, with red arrows denoting the coupling for each version. The coupling for MCEv2's outer coefficient uncouples the trajectories.

The key to the success of the MCE methods lie within the sampling techniques(69). The first techniques, trains, swarms and pancakes were previously established in CCS(2). Swarms are created by generating additional ‘satellite’ coherent states around a central ‘core’ initially generated coherent state with given shifts in position and momentum to create an interacting basis set that ensures the resulting propagation stays quantum and not semiclassical. The size of the swarm depends upon its compression parameter, and the optimal value differs for each individual case. In practice the core coherent state is not included and the compression parameter is varied and the swarm is recalculated until a swarm with an optimal norm is found. When the system has a few degrees of freedom that are more impactful to the wavefunction and overall dynamics, it is possible to use a smaller compression parameter for these than the less important bath modes, giving rise to a ‘stretched’ swarm, a pancake, that is capable of targeting the most important modes. When performing direct dynamics, the electronic information received from the electronic structure package is the most expensive part, while the nuclear trajectory propagation can be seen as practically free of cost in comparison. Therefore, the MCE methods employ ‘trains’ of basis functions which are multiple basis functions following the same trajectory with a shift in time, allowing reuse of the electronic structure information as it has already been calculated for a basis set in that exact area of phase space.

The final sampling technique is that of cloning, introduced firstly into MCEv2 as the method had problems with converging to the results produced by MCEv1 in several spin boson cases(69). Cloning rectifies a problem and the main downside of using Ehrenfest trajectories. Ehrenfest trajectories are cheap and stay coupled for a relatively long timeframe, being calculated from the mean potential of the potential energy surfaces, directing the basis functions to the relevant phase space. The issue arises if there are multiple electronic states that constitute a significant part of the configuration, where non-adiabatic coupling is low. In this case, the trajectories can be seen as ‘straddled’ between the electronic states and become unphysical, as a wavefunction is capable of splitting itself and exploring multiple regions of phase space at the same time, ultimately leading to misguiding of the basis sets and leading to inaccurate results. In the two-dimensional spin boson case, this condition can be calculated as the difference of the force experienced by the basis function from the 2 potential energy surfaces,

$$\Delta F_{1,n} = -\Delta F_{2,n} = |a_{1n}^* a_{2n}|^2 (\nabla_R V_1 - \nabla_R V_2) \quad (1.9)$$

In practice the condition can simply be said to be when the quantum amplitudes are equal due to the fact that the differential of each potential is constant (in the spin boson model) and therefore can be removed from the equation, with the threshold then becoming $|a_k^{(1)} a_k^{(2)}|^2 > 0.249$. Cloning then occurs whenever a problematic straddled basis function leaves such a region of low adiabatic coupling, replacing said basis function by two new basis functions, with one contained electronic contributed that the original basis function received from one singular electronic state, and the other contains the contribution from every other electronic state, causing the combination of the two new basis functions to have the exact same contribution to the overall wavefunction as before the cloning process. This idea of cloning and splitting the wavefunction is analogous to the spawning idea used in ab initio multiple spawning(70-73), a direct dynamics extension of full multiple spawning(74-76).

$$|\psi'_n\rangle = |\chi_n\rangle \left(\frac{a_I^n}{|a_I^n|} |\psi_I\rangle + \sum_{J \neq I} 0 |\psi_J\rangle \right) \quad (1.10)$$

$$|\psi''_n\rangle = |\chi_n\rangle \left(0 |\psi_I\rangle + \sum_{J \neq I} \frac{1}{\sqrt{1 - |a_I^n|^2}} a_j^n |\psi_J\rangle \right) \quad (1.11)$$

This process imitates the forking of the wavefunction and allows the Ehrenfest trajectories to remain a faithful representation, and this algorithm was implemented in the direct dynamics version of MCE, AIMC. AIMC is the current pinnacle of the MCE method and has been used to calculate the ab initio direct dynamics of photodissociation of different systems(77, 78), to capture quantum effects such as tunnelling(79), and has found success being implemented in the computational chemistry program NWchem(80). The best example of the use case of AIMC is in studying pyrrole molecules(81).

In the first AIMC paper investigating pyrrole, Makhov et al, showed that the cloning procedure can be used to generate a more detailed mechanism for the photodissociation, adding insights to an experiment generating a wave packet of excited pyrrole molecules via use of a pump pulse.

While the pump pulse from the probe in the experiment was limited to 120fs, the simulation through AIMC can take much smaller timesteps creating a much higher resolution of results than experiment alone, showing that 27 of the trajectories dissociate within 50fs after excitation. The discrepancies between the spectra generated by simulation and experiment were found to be due to the choice of the electronic structure package, and not the underlying method or theory of AIMC. This paper also shows the importance of the inclusion of the cloning algorithm as the cloned trajectories are able to follow the branching of the mechanisms of dissociation which allows the production of spectra with two main features, whereas MCE without cloning is only capable of producing the main peak for molecules such as imidazole(78).

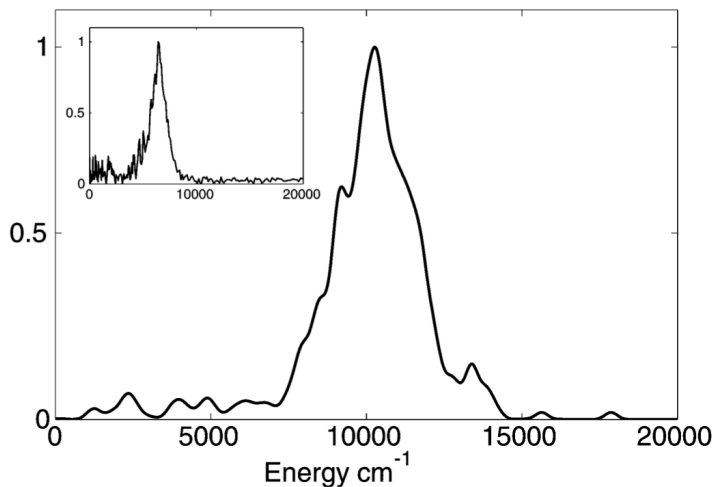


Figure 1.3: TKER spectra of pyrrole showing the bimodal presentation, only possible through the introduction of cloning. Calculated by AIMC, copied from reference 81.

In a following paper(82), the total kinetic energy release (TKER) spectra of both pyrrole and deuterated pyrrole were accurately generated and showed the shift to lower energy expected with the isotopic substitution. The method was also capable of analysing how the excitation of different vibrational modes would affect the photodissociation of the molecule, achieved by modifying the initial condition of the certain pre-excited modes, once again confirming experimental findings and chemical intuition of the selectivity of the molecule, in that only excitation of the N-H bond creates any notable change in the TKER spectra. Extracting the time of dissociation from the trajectory shows that the decrease in dissociation time caused by vibrational pre-excitation is a more pronounced effect in deuterated pyrrole than in hydrogen pyrrole(83), a somewhat unexpected result. This conclusion highlights how rigorous quantum methods can go beyond confirming past experimental results to inspiring or guiding new directions of exper-

imental research.

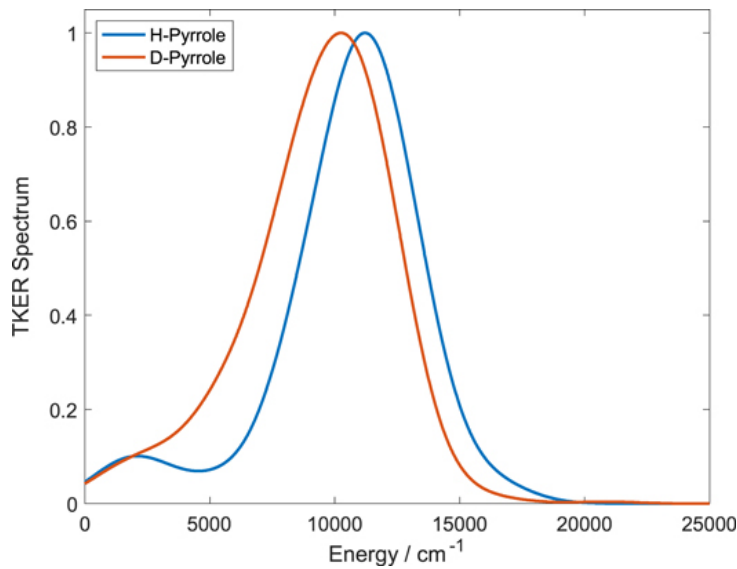


Figure 1.4: TKER spectra of both hydrogen and deuterated pyrrole. The isotopic shift is well accounted for as expected. Calculated by AIMC, copied from reference 82.

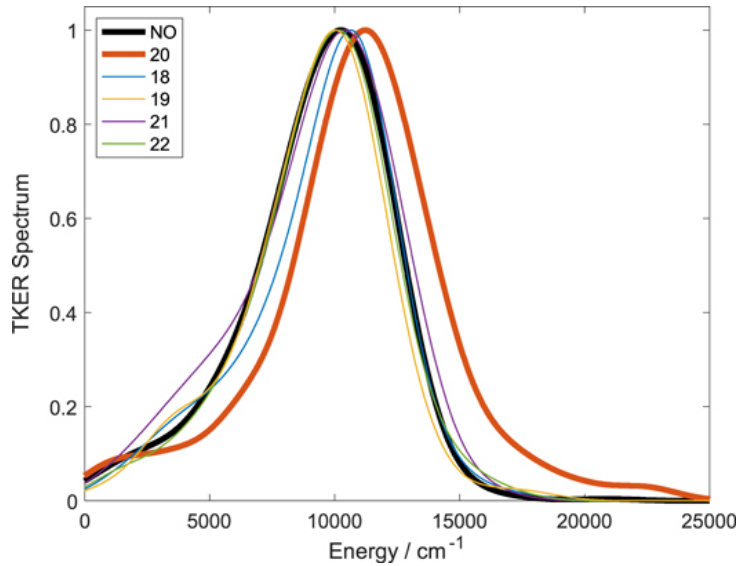


Figure 1.5: TKER spectra pyrrole after vibrational pre-excitation of different modes. Only mode 20 produces the shift to higher energy. Calculated by AIMC, copied from reference 82.

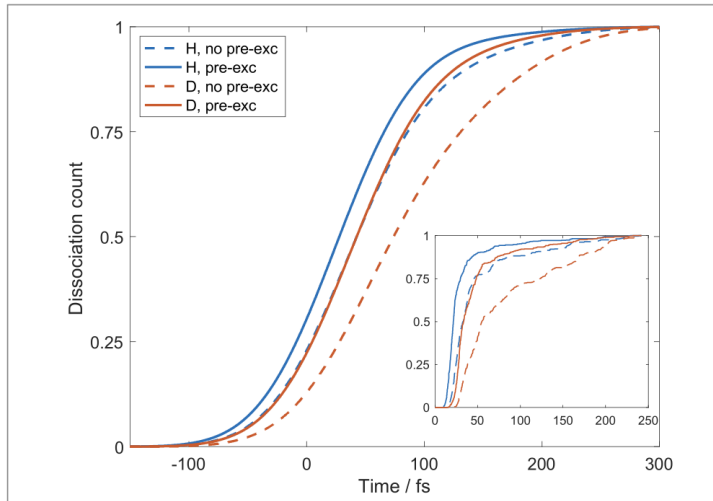


Figure 1.6: Graph showing the fraction of dissociation per femtosecond for hydrogen and deuterated pyrrole, depending on vibrational pre-excitation. Calculated by AIMC, copied from reference 82.

1.3 The spin boson models and methods to solve it

The spin boson model(84-86) is a simple yet versatile model to represent a variety of open quantum systems, consisting of two electronic potential energy wells coupled to a bath environment, and can represent different systems(87,88). The Hamiltonian of the spin-boson model is,

$$\hat{H} = \begin{bmatrix} H_B + H_C + \epsilon & \Delta \\ \Delta & H_B - H_C - \epsilon \end{bmatrix} \quad (1.12)$$

where ϵ represents the energy bias between the two potential energy surfaces, Δ represents the tunnelling parameter and H_B, H_C are the Hamiltonians of the bath and coupling between the system and bath respectively. All relevant information regarding the bosonic bath of the spin boson model can be found within the bath's spectral density function, and this review focuses on the Ohmic form where the power law relation between the spectral density and frequency is assumed to be linear until a chosen characteristic frequency, where an appropriate cut off function is chosen. The general Ohmic spectral density is,

$$J(\omega) = \frac{\pi}{2} \sum_m \frac{(C^{(m)})^2}{2(\omega^{(m)})^2} \delta(\omega - \omega^{(m)}) \quad (1.13)$$

The 3 most commonly studied cut off functions for the Ohmic spectral density are the exponential cut off(89), the Drude-Laurentz (Debye) cut off(90-92) and the underdamped brownian motion cut off(82,93,94). The exponential cut off assumes an exponential decay after the characteristic frequency, and the equation for the spectral density is often rewritten to include the Kondo parameter, which relates to the coupling strength between the system and the bath,

$$J_{exp}(\omega) = \frac{\pi}{2} \alpha_k \omega e^{-\omega/\omega_c} \quad (1.14)$$

The Drude-Laurentz has a less severe decay and thus the resulting spectral density has a much longer tail, causing the higher frequencies to become more relevant and impactful in calculations,

$$J_{DL}(\omega) = 2\pi\lambda\omega \frac{\Omega}{\Omega^2 + \omega^2} \quad (1.15)$$

The final cut off considered in this review is the underdamped Brownian oscillator, which is the least investigated of the 3 for the spin boson model. The underdamped oscillator can cause issues for certain methods due to the heavy oscillating nature and has a spectral density of the form,

$$J_{UBO}(\omega) = \frac{\Omega\gamma\lambda}{(\omega^2 - \omega_c^2) + \gamma^2\omega^2} \quad (1.16)$$

In general, the behaviour of the spin boson model can be qualitatively defined by three categories, damped oscillations, incoherent relaxation and relocalisation. Damped oscillation occurs when the bath and the system are not strongly coupled. As the coupling strength increases, the oscillations become fewer and less pronounced until the incoherent relaxation regime oc-

curs, showing an exponential decay to the equilibrium (a population difference of zero in the symmetrical well cases, $\epsilon = 0$). Relocalisation is a special regime that occurs at high coupling strength particularly at zero temperatures. With these parameters, relocalisation is a physical artefact where rapid initial population transfer occurs until a given population difference is reached where the population transfer then sharply reduces to 0. The MCE methods developed have been shown capable of simulation each of these dynamical regimes.

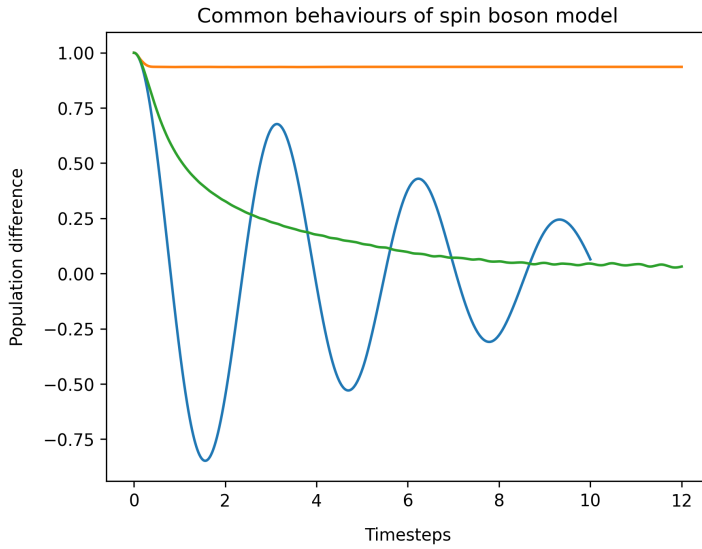


Figure 1.7: Graph showing the three most common behaviours of the spin boson model.

MCE is not the only method developed to solve the spin boson model. The multiconfigurational time dependent Hartree (MCTDH)(95-97) is a rigorous method of solving the spin boson model, which has previously served as a benchmark for MCE and other methods. MCTDH is a numerically exact variational method, making use of the efficiency of single-particle functions $|\varphi_{jk}^k(t)\rangle$, rewriting the overall wavefunction to be a combination of these single-particle functions,

$$|\psi(t)\rangle = \sum_J A_J(t) |\phi_J(t)\rangle = \sum_{j1} \dots \sum_{jm} A_{j1,j2,\dots jm}(t) \Pi_{k=1}^M |\varphi_{jk}^k(t)\rangle \quad (1.17)$$

These functions are chosen for their flexibility and their ability to represent multiple relevant Cartesian degrees of freedom within a single single-particle function, reducing the total number of configurations needed. However, the major downside to the MCTDH method is that it suffers from exponential scaling as it requires every configuration-interaction (CI) of every

single-particle functions, restricting the scalability of the method and preventing the method to be being applied to systems with large degrees of freedom. This downside can be somewhat rectified by constructing the single particle not through full CI but instead through a multiconfigurational expansion that develops through time, producing the multi-layer MCTDH method (ML-MCTDH)(66). In this approach the wavefunction is written in the same way but with the single-particle functions having a different formulation,

$$|\varphi_n^k(t)\rangle = \sum_i B_I^{k,n}(t) |u_I^k(t)\rangle \equiv \sum_{i1} \sum_{i2} \dots \sum_{iQ(k)} B_{i1,i2,\dots,iQ(k)}^{k,n} \Pi_{q=1}^{Q(k)(k,q)}(t) |v_{iq}^{(k,q)}(t)\rangle \quad (1.18)$$

and so the need for calculation of full CI is replaced by the computationally cheaper multiconfigurational time-dependent basis set expansion. The multi-layer aspect of this method comes from the fact that the new time-dependent function $|v_{iq}^{(k,q)}(t)\rangle$ can once again be expanded by another multiconfigurational expansion, and this technique can be applied as many times as needed, providing the method with recursive multiple layers. In order to retrieve information from this construction of the wavefunction, single hole functions are first defined. For the first layer the single hole function is explicitly calculated by the projection of any given single particular function onto the overall wavefunction,

$$|\Psi_n^k(t)\rangle = \sum_{j1} \dots \sum_{jk-1} \sum_{jk+1} \dots \sum_{jp} (t) A_{j1,\dots,jk-1,jk+1,\dots,jp} \Pi_{l \neq k}^p |\varphi_{jl}^l(t)\rangle \quad (1.19)$$

whereas for the subsequent layers, the single hole functions are found by exploiting the known relation to the layer 1 step above,

$$|g_{L(i),n,r}^{(k,q)}(t)\rangle = \sum_r |v_r^{(k,q)}(t)\rangle |g_{L(i+1),n,r}^{(k,q)}(t)\rangle \quad (1.20)$$

These functions are then used to calculate useful operators such as the mean-field operator and density matrices. The following equations given are for the first layer only,

$$p_{nm}^{(k)}(t) = \langle \Psi_n^k(t) | \Psi_m^k(t) \rangle \quad (1.21)$$

$$\langle \hat{H} \rangle_{nm}^{(k)}(t) = \langle \Psi_n^k(t) | \hat{H} | \Psi_m^k(t) \rangle \quad (1.22)$$

The equations of motion for the ML-MCTDH method can then for each layer be found applying the variational principle to the overall wavefunction with respect to the expansion coefficients defining that given layer,

$$i|\dot{\Psi}\rangle_{L1coeff}(t) = \hat{H}(t)|\Psi(t)\rangle \quad (1.23)$$

As each individual layer can be optimised it allows for the variational functional to become more flexible, assisting in the propagation of the wave packets and allowing the ML-MCTDH method to simulate a significantly higher number of modes than previously available to the method.

An area that often causes difficulty for the methods developed to solve the spin boson model is the zero-temperature regime. This is because at low temperatures, the quantum effects dominate the system causing difficulties for methods that rely on approximations, as the bath also has a longer memory time and the methods have to be capable of capturing the change between incoherent decay to relocalisation, as coupling strength increases.

A frozen Gaussian trajectory based method that was capable of producing accurate results in the zero-temperature regime is FMS(98). Unlike MCE, FMS uses a multi-set ansatz such that each electronic state has its own frozen Gaussian basis set,

$$\Psi = \sum_I \chi_I \varphi_I \quad (1.24)$$

The nuclear wavefunction consists of multiple coherent states. The coefficients that weight these

coherent states are given by,

$$\frac{dC^J(t)}{dt} = -i(S_{ll}^{-l}(H_{ll} - i\dot{S}_{II}C^I + \sum_{J \neq I} H_{IJ}C^J) \quad (1.25)$$

where the overlap matrices are as follows,

$$(S_{II})_{ki} = \langle \chi^{(I)_k} | \chi_i^{(I)} \rangle_R \quad (1.26)$$

$$(\dot{S}_{II})_{ki} = \langle \chi_k^{(I)} | \frac{\partial}{\partial t} \chi_i^{(I)} \rangle_R \quad (1.27)$$

and the Hamiltonian matrix has the elements,

$$(H_{IJ}) = \langle \chi_k^{(I)} \Phi_I | \hat{H} | \chi^{(J)} \Phi_i \rangle \quad (1.28)$$

A defining feature of the FMS is the use of an adaptive basis set through the spawning procedure, in a similar fashion to cloning in the MCE method. This allows FMS to begin propagation with a smaller basis set, and when a basis function travelling on one potential energy surface enters a region where it is strongly coupled to another, a second basis function is spawned on that potential energy surface, expanding the size of the nuclear basis set. The initial basis function, often referred to as the parent, and the spawned basis sets, often referred to as the child(ren), are required to have the same classical energy, position and momentum and due to the fact they are travelling on different potential energy surfaces will often spawn with a different velocity to the parent. The spawning procedure was initially developed in order to capture non-adiabatic effects; the spin boson model however is a diabatic model and therefore the coupling between the two potential energy surfaces is not localised to specific regions of time or space but is constant and defined by the Δ parameter. Therefore the spawning procedure had to be modified to

ensure that each basis function within the basis set has at least the minimal overlap with basis functions on the other potential energy surface. At every timestep, the overlap is calculated with every basis function on the other potential energy surface and if no overlap greater than the defined threshold is found then a child basis function is spawned to rectify this.

$$O_i = \text{Max}_j |\langle \chi^i | \chi^j \rangle| \quad (1.29)$$

This condition allows the basis set to correctly emulate the constant nature of the coupling between potential energy surfaces present in the spin-boson model, leading to the FMS method being capable of converging to accurate results even at zero temperature.

For example, a perturbative method that is used to solve the spin-boson model is the non-interacting blip approximation (NIBA)(98-101) that is normally restricted to weak coupling strengths ($0 < \alpha < 0.5$) as it is said to be exact at coupling values of $\alpha = 0$ and $\alpha = 0.5$, and near those values NIBA was shown to match other methods very well with agreement decreasing in the range between the two exact coupling strengths, showing unexpected difficulty even in the preferred regions of the method. NIBA has also been found to have difficulties simulating population exchange of systems with very low characteristic frequency with a Debye spectral density, but has been shown to compare well with MCTDH at zero temperatures(102) for large characteristic frequency, particularly when the system is approaching the scaling limit, where the characteristic frequency ω_c far exceeds the tunnelling parameter Δ and the oscillation becomes somewhat predictable.

It is common for methods to developed firstly to tackle certain cases and later expanded upon or improved in order to solve low temperature cases. One such method often applied to the spin boson model is the Hierarchical equations of motion (HEOM)(103). The HEOM method works by rewriting the density matrix of the system into the hierarchical form and propagating. Originally the method of HEOM was best suited to the Drude-Laurentz spectral density, as it relies on the specific decomposition of the bath correlation function in order to generate the equation of motion, limiting both the choice of spectral densities and temperature ranges. In order to properly manage the demands of the zero temperature, HEOM has different extensions(104) and revisions of correction terms. Recently, the method has been reformulated(105) to remove

the requirement of the exponential functions in the bath correlation function and now employs a number of different truncation techniques in order to better suit the system, and HEOM has found application to a multitude of systems beyond the spin-boson model(106-109).

Because MCE methods have only been applied to the ohmic spin boson case, the ohmic cases of the model have been the focus of the review, but there is ongoing research into sub-ohmic cases(110-113). However there are methods that are capable of treating both ohmic and sub-ohmic modes,such as unitary transform methods(114,115), semiclassical surface hopping(116), NIBA and MCTDH(117). As before in the ohmic case, NIBA has regimes where it miss estimates the dynamics of this system and only certain conditions where it can match the calculations of MCTDH (when the characteristic frequency is very large). MCE's versatility in both the sub-ohmic and super-ohmic region is yet to be tested and remains a potential direction for research.

Chapter 2

Current work

Given the pivotal role the cloning procedure played in increasing the convergence of MCEv2 and producing accurate results for real systems with AIMC, it is theorised that successful implementation of cloning into MCEv1 will assist in converging the final cases of the spin boson model that have proven difficult for the model.

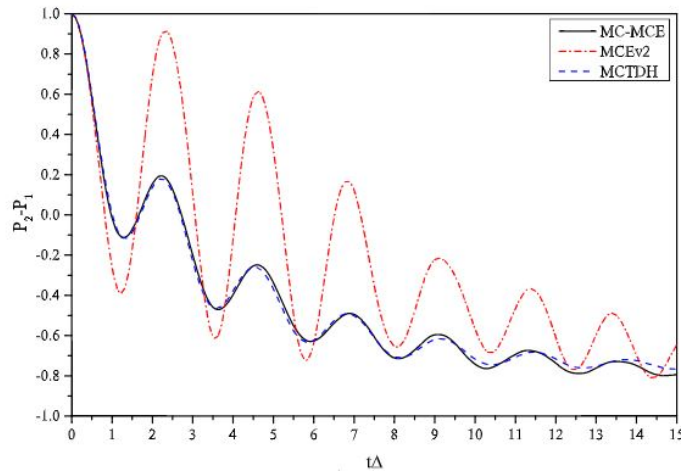


Figure 2.1: Comparison of the MCEv2 method with and without cloning for the asymmetrical well case. MCTDH is also provided as a benchmark. Copied from reference 69

MCEv2 independent classical trajectories allow for the monitoring of each individual basis function and spawning of clones on any particular timestep where the contributions from each potential energy surface are roughly equal. MCEv1's coupled Ehrenfest trajectories while helping propagation and allow for overall fewer basis functions, has the disadvantage of not allowing the basis functions to be too close together in phase. As cloning involves creating two basis functions with exactly identical phase space co-ordinates, the cloning procedure as implemented

in other versions of the methods. Instead the entire wave function has to be cloned, essentially doubling the size of the basis set, and both clones are propagated separately to completion before being recombined to recover the behaviour of the system. At the timestep of cloning the wavefunction is split into two bundles, which each bundle containing the entirety of the contribution from one potential energy surface,

$$\begin{aligned} |\Psi(t)\rangle = \sum_{k=1,N} (a_k^{(1)}|1\rangle + a_k^{(2)}|2\rangle)z_k(t)\rangle &= \sum_{k=1,N} (a_k'^{(1)}|1\rangle + 0|2\rangle)z_k(t)\rangle \\ &\quad + \sum_{k=1,N} (0|1\rangle + a_k''^{(2)}|2\rangle)z_k(t)\rangle \end{aligned} \tag{2.1}$$

As in MCEv2, at the time of cloning the summation of both clones yields the original basis set and so cloning can be performed without perturbing the overall system wavefunction. As MCEv1 does not need to enforce a normalisation condition, the clones can propagate containing only fractal population. The two bundles are then propagated separately using the usual MCEv1 working equations before undergoing retroactive recombination,

$$P_{1,tot} = P_1' + P_1'' \tag{2.2}$$

$$P_{2,tot} = P_2' + P_2'' \tag{2.3}$$

where the index ' denotes whether the population belongs to clone 1 or 2. Population in the MCE methods are calculated as,

$$P_i' = \sum_k \sum_j a_{ik}'^* a_{ij}' \langle z_k' | z_j' \rangle \tag{2.4}$$

However when cloning was implemented as in equation 2.1, the change in basis set does in fact perturb and in most cases, completely derails propagation preventing generation of population

dynamics even in cases that MCEv1 previously performed extremely well.

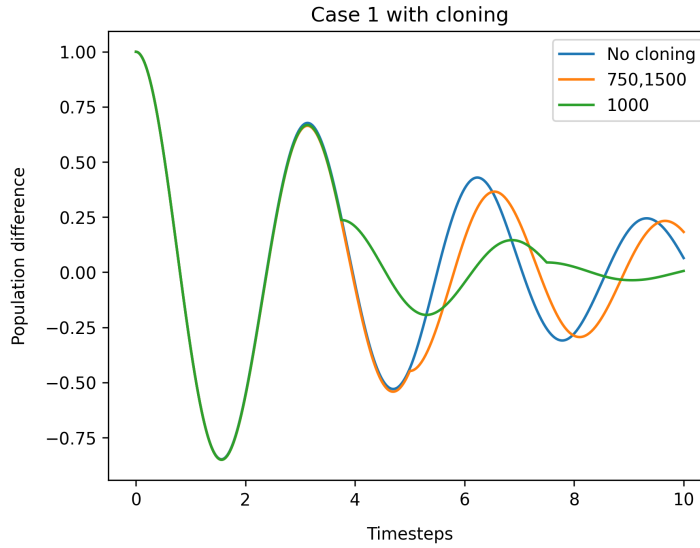


Figure 2.2: Population difference for a symmetrical well case with exponential cutoff with parameters $\omega_c/\delta = 2.5$, $\alpha_k = 0.09$, $\epsilon=0$, $\beta\delta=5$. Results calculated with MCEv1 with $N_{rpts} = 32$ repeats and $M = 50$ bath modes and $N_{bfs} = 50$. The number of cloning events was varied.

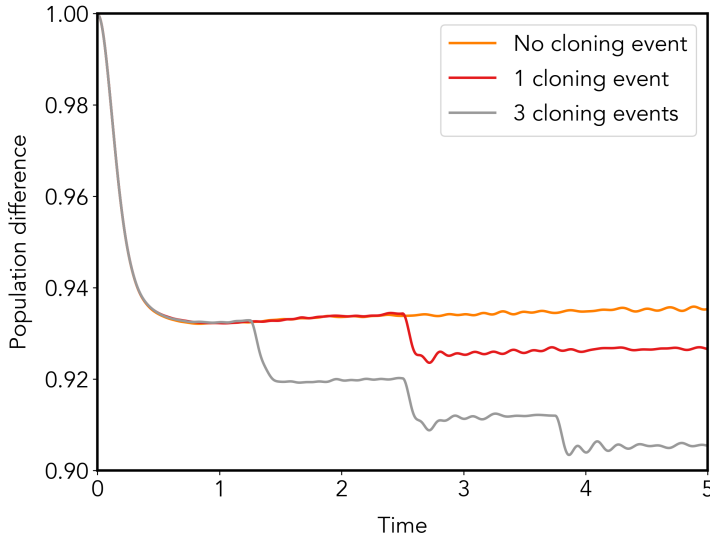


Figure 2.3: Population difference calculated by MCEv1 at zero-temperature. Symmetrical well case with parameters $\omega_c/\delta = 10$, $\alpha_k = 1.5$, $\epsilon=0$, $\beta\delta=1000$ (a suitable estimation of infinity is required). All runs consisted on $N_{rpts} = 128$ repeats and $M = 200$ bath modes and $N_{bfs} = 50$. The number of cloning events were varied for each run.

The above figures are perfect examples of how this implementation of cloning fails. Figure 2.2, the symmetrical well case is a 'trivial' spin boson case that can be solved by the MCE methods with relatively few basis functions and bath modes. However when the cloning procedure is performed when the population difference is approximately 0, i.e. the potential energy states

are equally occupied, the propagation difference no longer oscillates as expected and instead produces an almost flat continuation. This is due to the clones essentially restarting propagation as they once again contain contribution from only 1 potential energy surface as in the initial conditions. This causes both clones to undergo the exact same change as at the beginning of the propagation, but as the total population of each clone is approximately equal, the population exchange becomes equal but opposite, cancelling out in the recombination phase.

Figure 2.3 is further evidence of this theory as it shows a zero-temperature strong coupling case exhibiting the relocalisation phenomenon. In this case, whenever cloning occurs, the population difference drops again in the same manner as the initial relocalisation. The extent to which the population drops also appears to be smaller with every cloning event, which is explained by the fact that the clone that contains all of the population of state 1 is smaller and makes up a smaller proportion of total population, leading it to dominate the final behaviour to a lesser extent.

The explanation for this behavior is that the clones were assumed to be independent once separated and that they could propagate freely before being recombined at the final timestep. This approach neglects quantum interference that takes place between the two clones that need to be taken into account. This can be done so by including the extra interactions in the recombination step,

$$P_{1,tot} = \frac{P'_1 + P''_1 + P'^{-''}_1 + P''^{-'}_1}{P'_1 + P''_1 + P'^{-''}_1 + P''^{-'}_1 + P'_2 + P''_2 + P'^{-''}_2 + P''^{-'}_2} \quad (2.5)$$

$$P_{2,tot} = \frac{P'_2 + P''_2 + P'^{-''}_2 + P''^{-'}_2}{P'_1 + P''_1 + P'^{-''}_1 + P''^{-'}_1 + P'_2 + P''_2 + P'^{-''}_2 + P''^{-'}_2} \quad (2.6)$$

The normalisation here is required as the clones are propagated in isolation and already sum to 1, and the post calculated interaction terms do not impact their values. The interaction terms have a similar form to the calculation population within the bundles meaning no additional information needs to be tracked and propagation can still occur separately with recombination after the final timestep,

$$P_i'^{-''} = \sum_k \sum_j a_{ik}'^* a_{ij}'' \langle z_k' | z_j'' \rangle \quad (2.7)$$

$$P_i''^{-'} = \sum_k \sum_j a_{ik}''^* a_{ij}' \langle z_k'' | z_j' \rangle \quad (2.8)$$

Despite the fact this version of cloning is significantly more expensive, it is possible for the cloning procedure to be called more than once per propagation, causing another doubling of the bundles and further increase in the number of interaction terms, as all clones generated from a single original basis set will continue to interact. In order to present the equations for interactions, it is best to adopt the notation of cross-terms detailing the interactions between the different clones to be,

$$CT^{\langle 1|2 \rangle} = CT_1^{\langle 1|2 \rangle} + CT_2^{\langle 1|2 \rangle} \quad (2.9)$$

$$CT_i^{\langle 1|2 \rangle} = CT_i^{\langle 1,2 \rangle} + CT_i^{\langle 2,1 \rangle} \quad (2.10)$$

$$CT_i^{\langle 1,2 \rangle} = \sum_k \sum_j a_{ik}^{1*} a_{ij}^2 \langle z_k^1 | z_j^2 \rangle \quad (2.11)$$

$$CT_i^{\langle 2,1 \rangle} = \sum_k \sum_j a_{ik}^{2*} a_{ij}^1 \langle z_k^2 | z_j^1 \rangle \quad (2.12)$$

The total population calculated from more than 2 clones is then,

$$P_{Total} = \frac{P_1^1 + P_2^1 + P_1^2 + P_2^2 + P_1^3 + P_2^3 + P_1^4 + P_2^4 + CT^{\langle 1|2|3|4\rangle}}{P_1^1 + P_2^1 + P_1^2 + P_2^2 + P_1^3 + P_2^3 + P_1^4 + P_2^4 + CT^{\langle 1|2|3|4\rangle}} \quad (2.13)$$

where the extended cross-term is given as,

$$CT^{\langle 1|2|3|4\rangle} = CT_1^{\langle 1|2|3|4\rangle} + CT_2^{\langle 1|2|3|4\rangle} \quad (2.14)$$

$$CT_i^{\langle 1|2|3|4\rangle} = CT_i^{\langle 1|2\rangle} + CT_i^{\langle 1|3\rangle} + CT_i^{\langle 1|4\rangle} + CT_i^{\langle 2|3\rangle} + CT_i^{\langle 2|4\rangle} + CT_i^{\langle 3|4\rangle} \quad (2.15)$$

Cloning with cross-terms has been shown to be effective in recovering the propagation of the spin boson cases studied in the first MCEv1 paper(56).

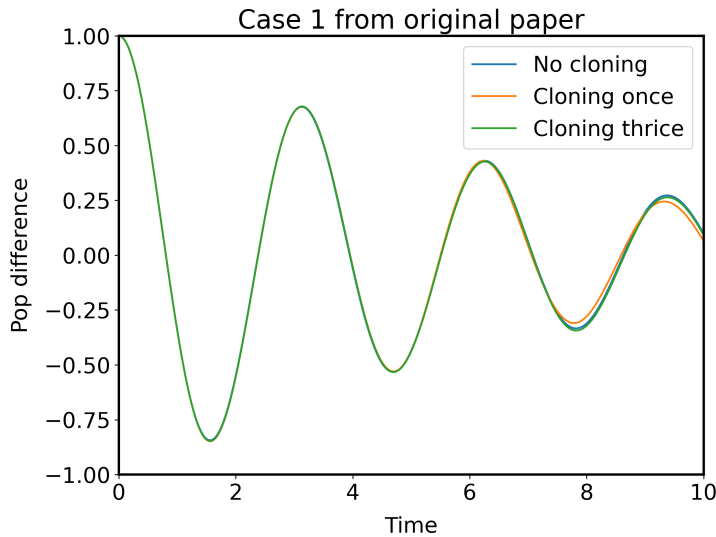


Figure 2.4: Population difference for a symmetrical well case with exponential cutoff with the same parameters as Figure 2.2. Cloning once (orange) occurred at timestep 1000, and the cloning thrice (green had cloning events at timesteps 500,1000,1500). The propagation with 3 cloning events matches perfectly the original converged MCEv1 result(blue).

Figure 2.4 is the same 'trivial' spin boson case as figure 2.2 and demonstrates that not only is cloning with cross-term interaction is viable and capable of recovering behaviour of propagation. It also shows that multiple cloning events can occur not only without perturbing the

propagation but that an additional cloning event can correct the small inaccuracies caused previously. Different placement and frequencies of the cloning event can produce slightly different final propagations, showing the versatility of the procedure.

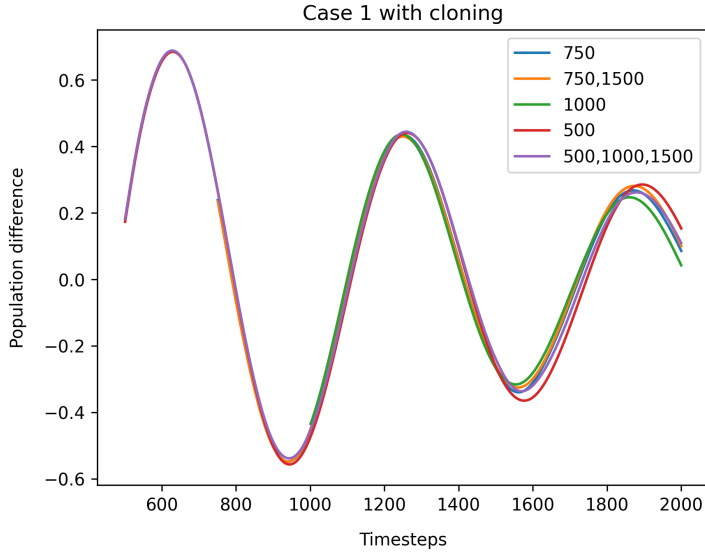


Figure 2.5: Population difference after cloning for the symmetrical well case shown in Figure 2.2. The number in the legend denotes the timestep(s) for the cloning event(s) for each propagation.

Figure 2.5 shows only the information produced involving cross-terms (i.e. only the propagation after a cloning event) as any propagation before a cloning event will be identical across all examples. The fact that the combination of cloning events leads to a scattering of final population difference, cloning is therefore not forcing a definitive underestimation or overestimation of population and in the case of cloning at time 500, can slightly shift the oscillation to be out of phase with the other propagations, and therefore the position of cloning is quite sensitive. This behaviour can also be seen in propagations with cloning events of different amounts or timestep placement. In order to better understand the mechanics of the cloning procedure, it is imperative to investigate the exact behaviour of the cross terms. The information regarding the evolution of the cross terms for several cases is shown below,

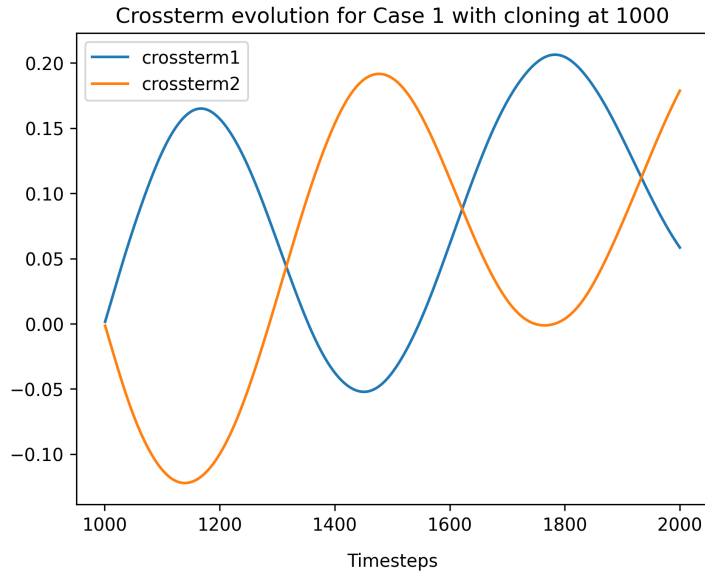


Figure 2.6: The evolution of cross terms throughout a propagation with the same parameters as Figure 2.2 with a cloning event at timestep 1000 out of a total of 2000 timestep.

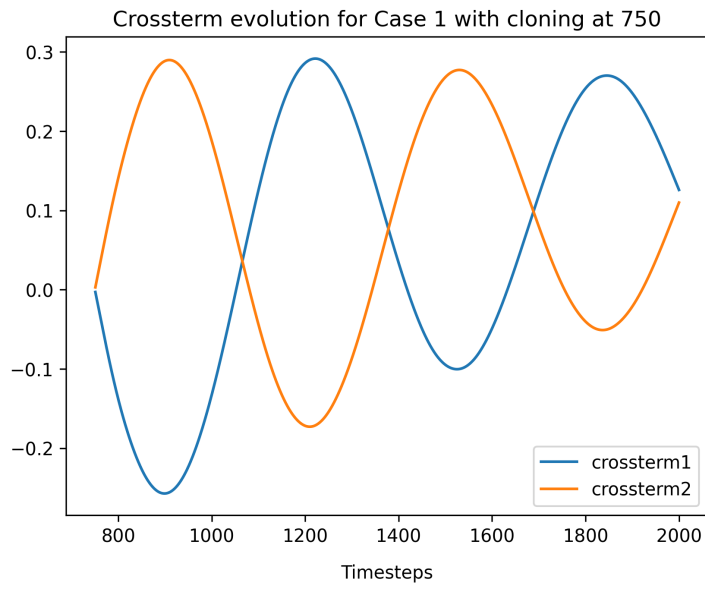


Figure 2.7: The evolution of cross terms throughout a propagation with the same parameters as Figure 2.2 with a cloning event at timesteps 750 out of a total of 2000.

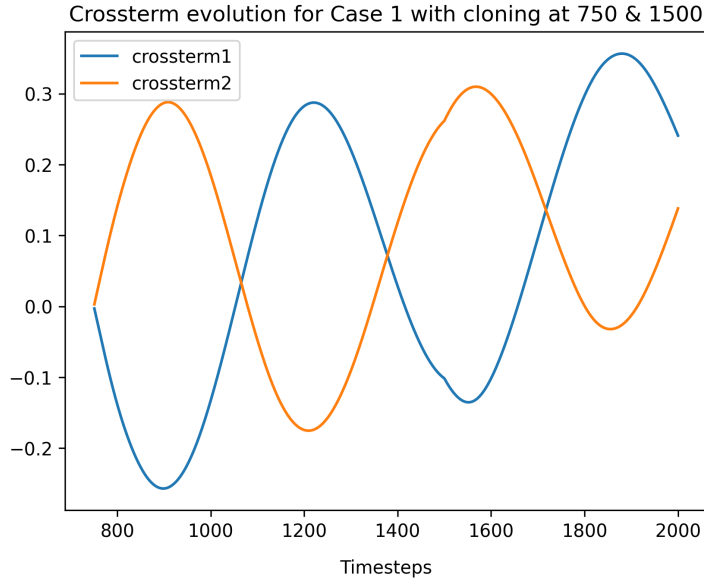


Figure 2.8: The evolution of cross terms throughout a propagation with the same parameters as Figure 2.2 with cloning events at timesteps 750 and 1500 out of a total of 2000.

The cross-terms follow an oscillating pattern, initially evolving in an opposite but equal manner. After the first cycle, the oscillation persists but both cross-term 1 and 2 begin to rise in value with the cross-term that is passing from higher to lower increasing at a much faster rate. This behaviour can be explained by the cross-terms recovering the oscillatory behaviour of the system that can be lost after cloning. The increase from the first peak to the second peak in cross-term 1 is an increase of less than 0.05, but the increase between the first and second trough is approximately 0.10. Interesting to note is that due to change in population difference at timesteps 750 and 1000, the initial cross-term that increases is different, with the cross-term that increases first corresponding to the state which is due to increase in population, as intuitively expected. Due to formulation of the equations for multiple cloning events, the cross-terms at the timestep of cloning are exactly equal before and after the creation of more clones as shown in Figure 2.8, however the oscillation of the cross-terms becomes slightly perturbed and causes a sharp increase/decrease before returning to normal evolution. The re-scale factor, how much the populations need to be divided by after inclusion of cross-terms in order to be re-normalised can also be plotted,

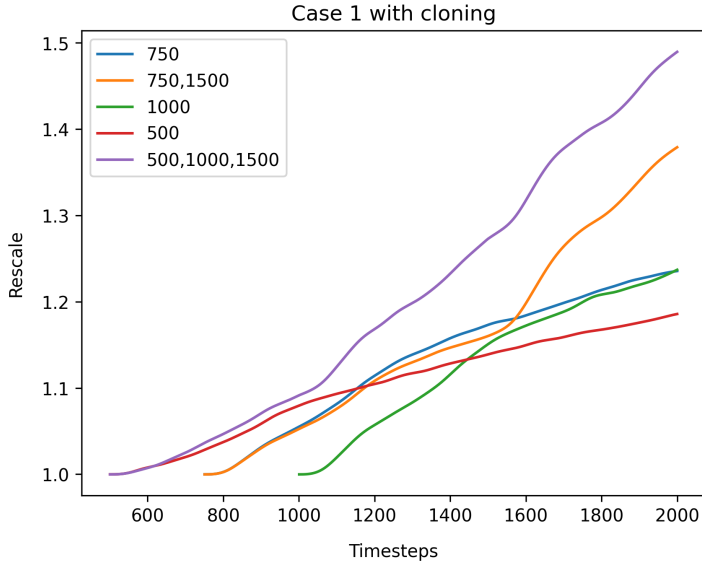


Figure 2.9: The normalisation re-scale factor shown for each of the different propagations shown in figure 2.5.

As the general increase in the value of the cross-terms suggest, the re-scale factor can be seen as a monotonic function. The gradient of the re-scale factor increases sharply with respect to cloning events, with the two outliers of highest final re-scaling factors having 2 and 3 cloning events.

Cloning with cross-terms can also be applied to relocalisation cases and recovers behaviour without causing the relocalisation, and can be shown to have a positive effect even with very few repeats. However, more interestingly the relocalisation does occur if the cloning procedure is applied any point where the population difference is stationary, i.e. after the initial population drop. This provides the best example of the current limits of cloning with cross-terms and shows it remains a precise tool and requires to be called at an optimal timestep in order to generate desired behaviour and results.

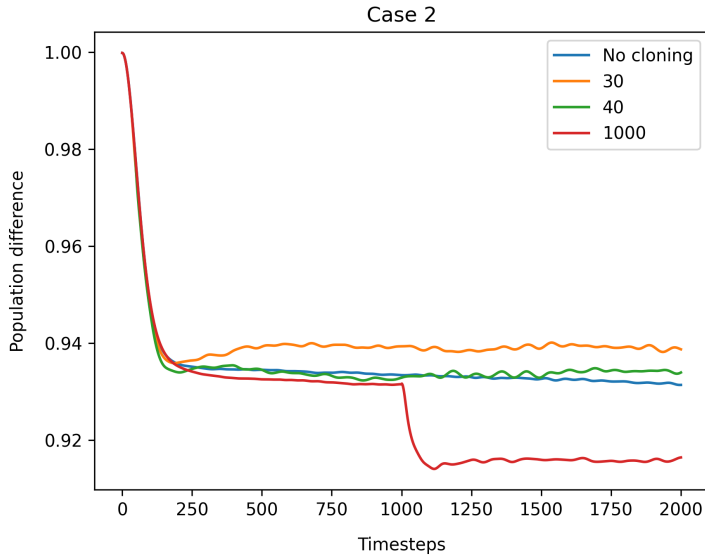


Figure 2.10: Relocalisation case with parameters $\omega_c = 10$, $\beta = 5000$ (as an estimation of infinity), $\alpha_k = 1.5$. The propagations were run with $N_{bfs} = 200$ and $M=200$ but with only 16 repeats. The number in the legend denotes the timestep of the cloning event

While cloning with cross-terms was capable of converging to the correct result as long as the cloning occurred early enough in the propagation, the cross-terms did not evolve in the same manner as the symmetrical well damped oscillation case. In the case of cloning at timestep 1000, the inclusion of cross-terms does not appear to be an improvement and the cloning event still induces a significant population drop.

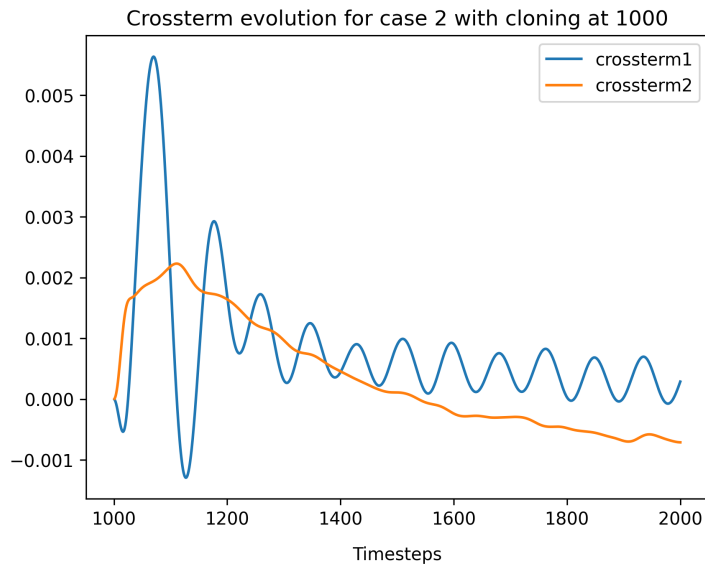


Figure 2.11: The evolution of cross terms throughout a propagation with the same parameters as Figure 2.10 with a cloning event at timestep 1000 out of a total of 2000.

This demonstrates a weakness of cloning with cross-terms as in the limit of cross-terms going to

0, the old cloning method is recovered. This is why even when cross-terms are included after the cloning event at timestep 1000, the resulting propagation is almost identical, as the size of the cross-terms barely exceed 0.005. Therefore it is clear that the introduction of cross-terms cannot always recover the correct propagation when cloning without cross-terms was too immediately destructive.

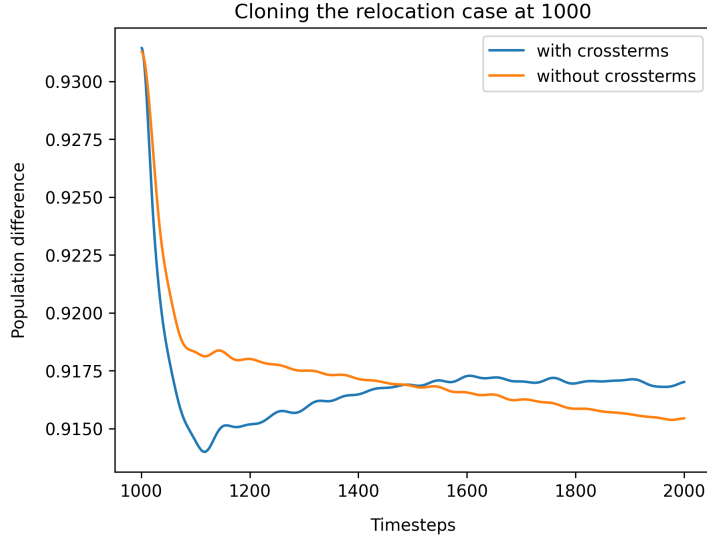


Figure 2.12: Population difference of case 2 with and without the inclusion of cross-terms after a cloning event at timestep 1000 of 2000.

For the two propagations shown that were capable of producing reasonably accurate results, the cross-terms have a slightly different evolution as well as larger magnitudes. Cross-term 1 takes an oscillatory form, while cross-term 2 has a sharp increase before decaying. However, the initial evolution of the cross-terms is still equal but of opposite sign, though this pattern is broken in fewer timesteps than before.

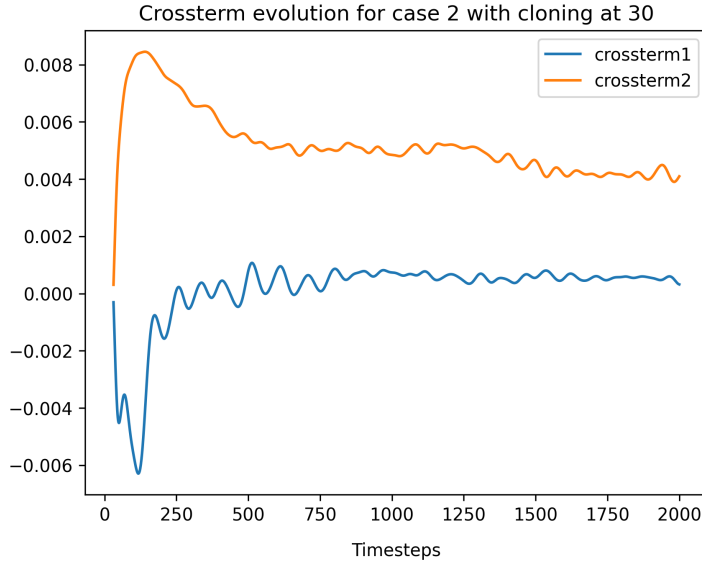


Figure 2.13: The evolution of cross terms throughout a propagation with the same parameters as Figure 2.10 with a cloning event at timestep 30 out of a total of 2000.

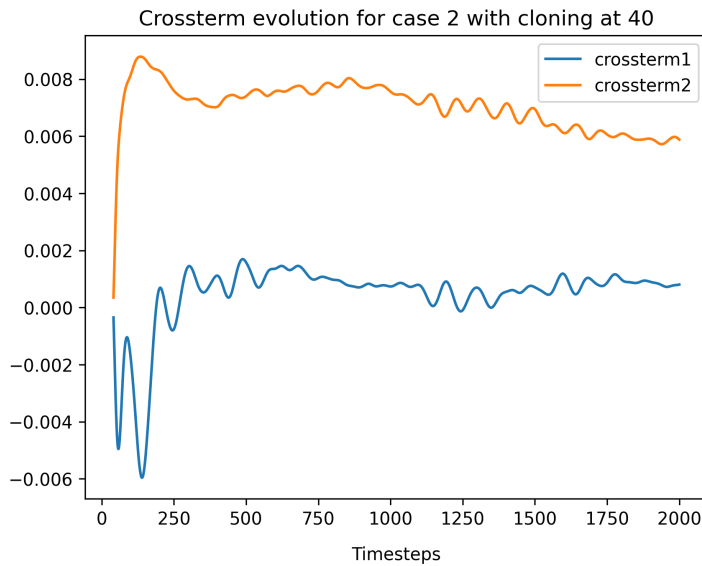


Figure 2.14: The evolution of cross terms throughout a propagation with the same parameters as Figure 2.10 with a cloning event at timestep 40 out of a total of 2000.

For both cases the cross-terms are very similar in terms of both evolution and magnitude which can be expected due to the cloning event occurring in the same region. However even though the cross-term evolution appears to be the indifferent between cloning at timestep 30 or 40, the resulting population difference is notable. When cloning at timestep 30, the propagation difference increases once it reaches the equilibrium population difference whereas cloning at timestep 40 resulted in a more stagnant population difference, even when compared to the propagation

without cloning. The oscillations appear to be stronger in propagations with cloning, but they can be removed by increasing the number of basis functions or repeats. Despite being of a much lower magnitude than in Case 1, the cross-terms were vital in achieving the correct stationary population, as the correction needed was also of a much lower magnitude. For cloning at both timesteps 30 and 40, cross-terms are required to reach the correct population after relocalisation with cloning without cross-terms stopping the sharp decay earlier before slowly decaying for the rest of the propagation.

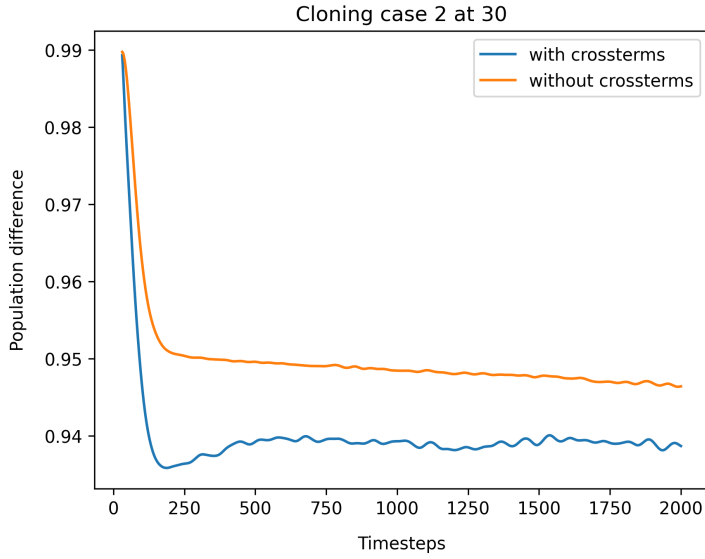


Figure 2.15: Population difference of case 2 with and without the inclusion of cross-terms after a cloning event at timestep 30 of 2000.

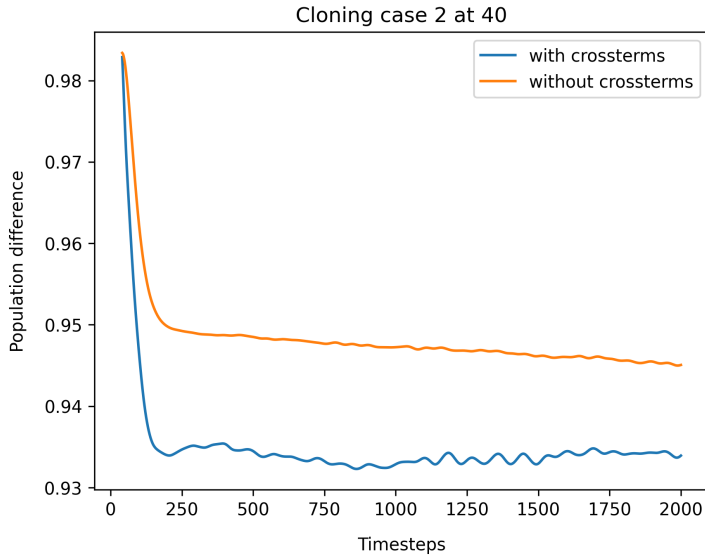


Figure 2.16: Population difference of case 2 with and without the inclusion of cross-terms after a cloning event at timestep 30 of 2000.

The last preliminary case investigated after the introduction of cross-terms was a propagation concerning incoherent relaxation. This system poses a similar challenge to the cross-terms as with relocalisation as there are no oscillations to recover, but instead a constant decay until equilibrium temperature has been achieved at the end of propagation. Therefore after cloning, the correct rate of decay needs to be maintained as well as finalising at the correct equilibrium.

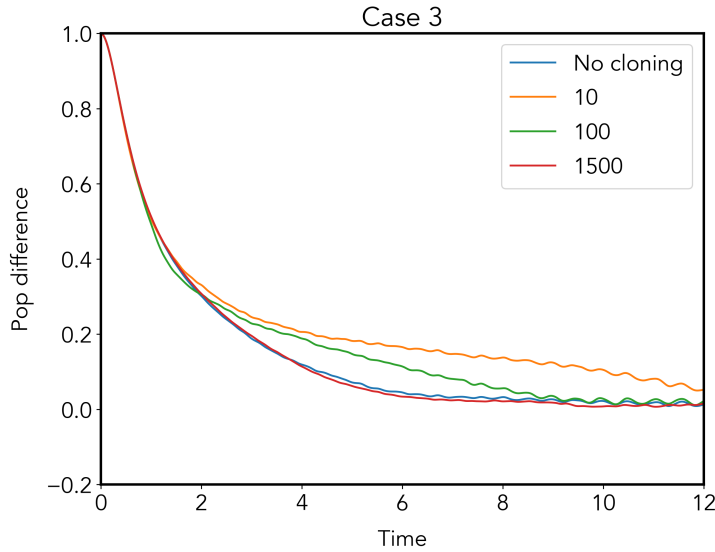


Figure 2.17: Incoherent relaxation case with parameters $\omega_c = 7.5$, $\alpha_k = 0.6$, $\beta = 5$ and $\epsilon = 0$. The propagation was ran with 200 basis functions and 200 bath modes. The number in the legend denotes the timestep of cloning.

In this case, cloning in the initial regions of propagation causes a heavily misguided rate of decay and in the earliest cloning event the final population difference is raised above the true equilibrium position of equal population of states. Cloning in the later regions however appears to be the correct decision as the propagation continues almost unperturbed, something that could be improved with more experimenting with the exact timestep of cloning.

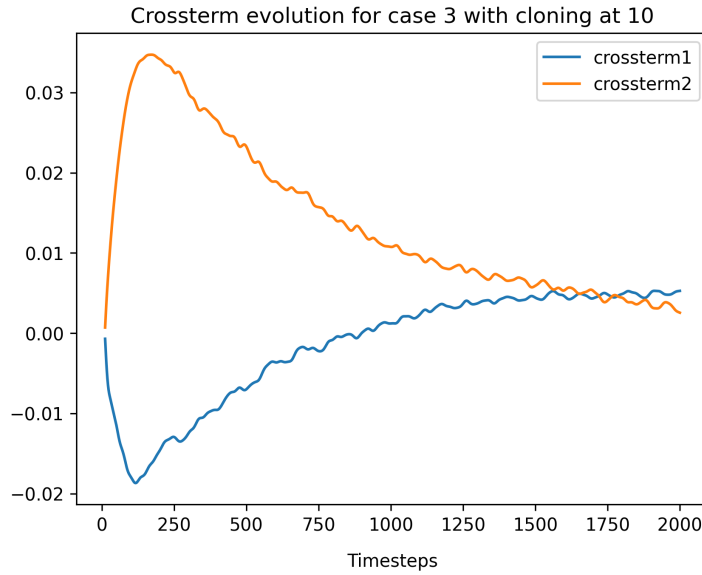


Figure 2.18: The evolution of cross terms throughout a propagation with the same parameters as Figure 2.17 with a cloning event at timestep 100 out of a total of 2000.

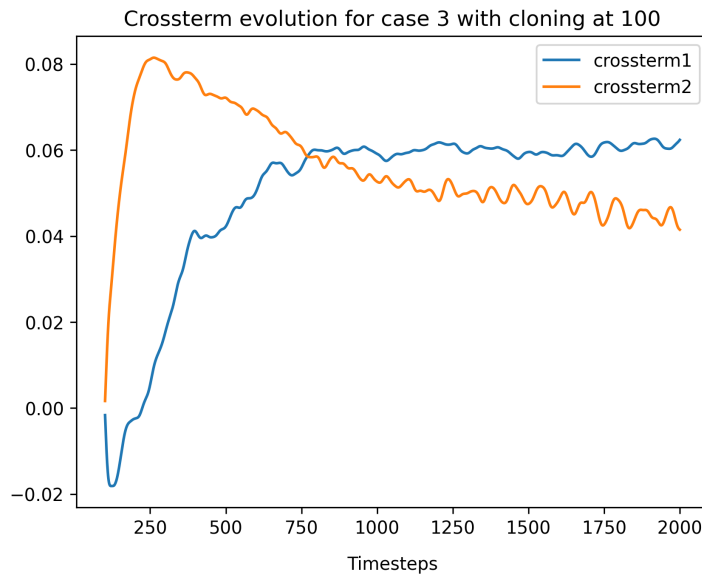


Figure 2.19: The evolution of cross terms throughout a propagation with the same parameters as Figure 2.17 with a cloning event at timestep 100 out of a total of 2000.

As expected cross-term 2 is initially the more positive as cloning is taking place when population 1 is higher than population 2. Cloning at timestep 100 shows that the change in decay rate is due to the initial behaviour of the cross-terms, where cross-term 2 increases and as always for the first timestep cross-term 1 evolves in an equal but opposite manner.

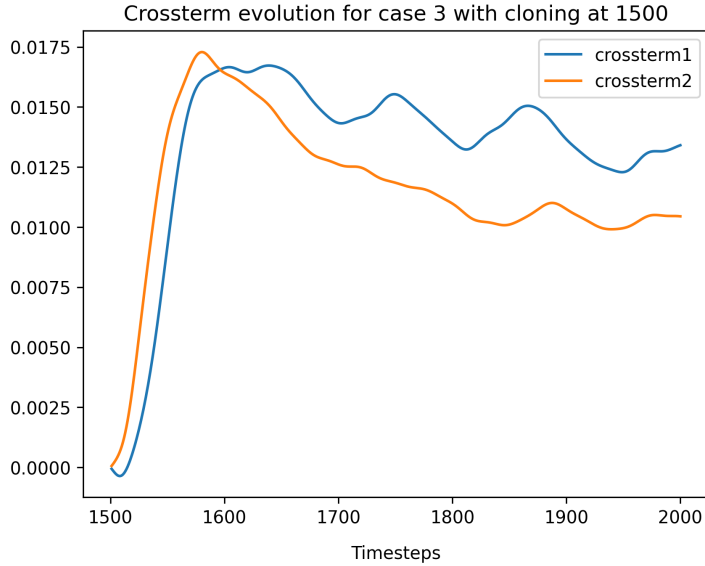


Figure 2.20: The evolution of cross terms throughout a propagation with the same parameters as Figure 2.17 with a cloning event at timestep 1500 out of a total of 2000.

Cloning at timestep 1500 shows that once the propagation begins to flatten out the drop in population difference is less severe than in case 2, as the population difference at the timestep of cloning and has an impact on the behaviour of the 2 clones without taking into account the interaction terms. Therefore while in case 2 cloning in the regions of slow population exchange induces the relocalisation, here it is advantageous as cloning maintains the correct final population difference. Cloning later in the propagation also has the benefit of being computationally much cheaper as propagation of the additional clone is the same cost as creating an additional repeat at that given timestep, with additional costs required to then calculate the cross-terms, making later cloning events preferable.

In later cloning events of case 3, cross-term 1 almost immediately begins to increase in line with cross-term 2. The crossing of the cross-terms however does still occur and cross-term 1 maintains the higher of the two at the final time step. However despite the patterns being similar, the magnitudes of the cross-terms are different by a factor of 3. This is because at timestep 1000, a significant proportion of the decay has already occurred and therefore the remaining population change is much less than cloning earlier in the propagation. While cross-terms of this magnitude cannot cause radical changes, the cross-terms are still useful.

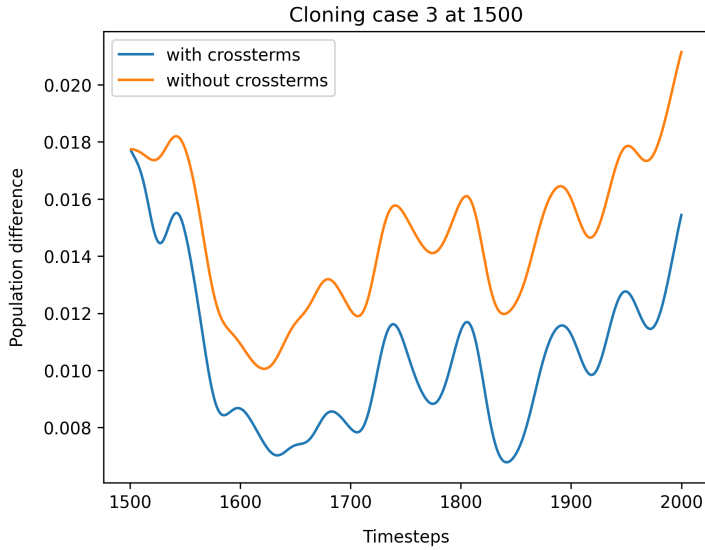


Figure 2.21: Population difference of case 3 with and without the inclusion of cross-terms after a cloning event at timestep 1500 of 2000.

While the difference between the propagations with or without cloning is within 0.02, it is reassuring to note that the cross-terms shift the population difference in the correct direction, and therefore overall cross-terms have not worsen clones that already producing correct propagations.

Cloning has been shown to recover behaviour from cases that MCEv1 was already capable of converging to the correct result. It is also important that cloning be shown to be a benefit for the few cases that remain to be fully converged. For this, several zero temperature cases have been investigated. As with the other methods covered at the end of chapter 1, MCEv1 without cloning can accurately produce several cases with different parameters.

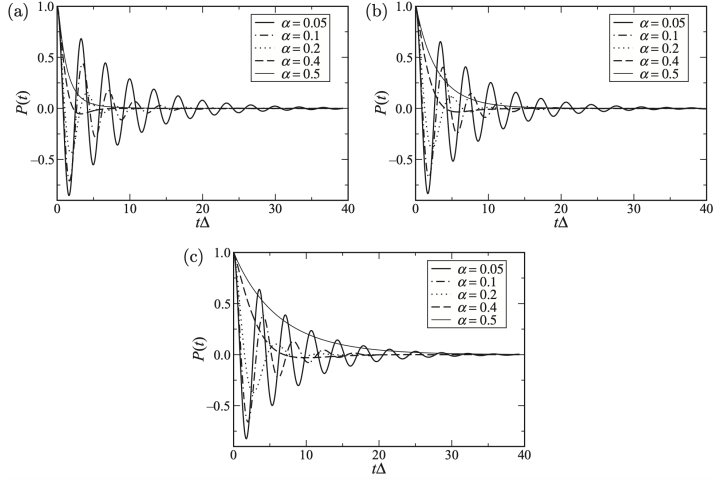


Figure 2.22: Figure 1 copied from reference 101 to serve as a benchmark. The coupling strength α is given by the legend of each graph. Graph (a), (b), (c) have the characteristic frequencies $\omega_c = 10/20/40$ respectively at 0 temperature.

For medium to high characteristic frequencies (ω_c between 10 and 40) and low coupling (α between 0.05 and 0.2), MCEv1 is capable of producing the damped oscillating decay correctly, but as coupling increases MCE struggles to match the transition to incoherent decay and incorrectly estimates the final populations, and with higher characteristic frequencies the final population equilibrium of symmetrical well cases is weighted towards the second potential energy well (the one that is not populated initially at time 0) for symmetrical well cases.

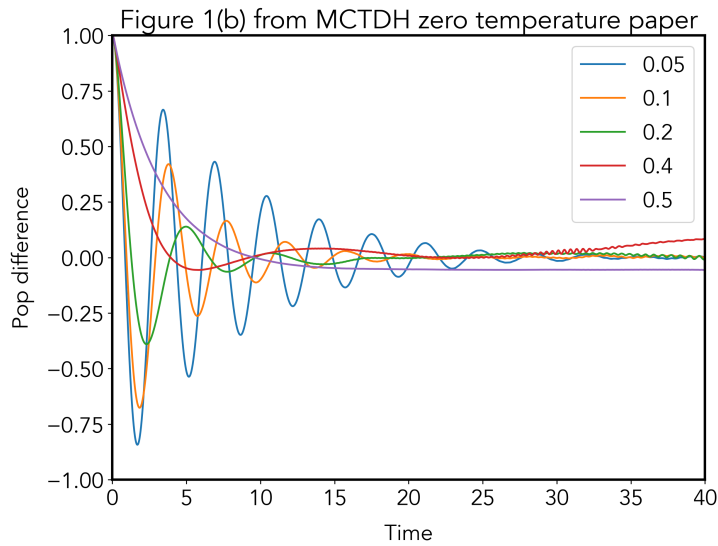


Figure 2.23: Cases from figure 2.23 b run with parameters $\omega_c = 20$, $\beta = 5000$ (to estimate infinity) and α_k ranging from 0.05 to 0.5. Propagation were carried out at $N_{bfs} = 200$, $M = 500$ and with 64 repeats.

For the characteristic frequency, $\omega_c = 20$, the cases with the lowest kondo parameter are con-

verged correctly. For the last two cases, with $\alpha = 0.4, 0.5$, the final population difference is overstated and understated respectively. In the cases where MCEv1 is already sufficient to converge, cloning with cross-terms can be shown to be non-destructive.

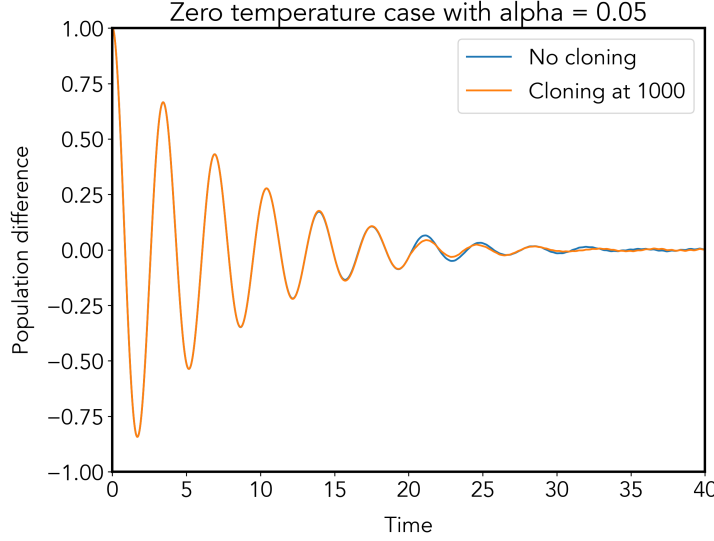


Figure 2.24: Cases from figure 2.23 b run with parameters $\omega_c = 20$, $\beta = 5000$ (to estimate infinity) and α_k ranging from 0.05 to 0.5. Propagation were carried out at $N_{bfs} = 200$, $M = 500$ and with 64 repeats.

Current investigation is searching for ideal cloning conditions for the cases where MCEv1 does not converge correctly without cloning. In order to improve the efficiency of this search, the idea of conditional cloning is being explored. A key contribution to the success of the cloning algorithm in AIMC is the existence of a condition that rectifies issues that can occur while the propagation is being calculated. Finding such an automatic, easily calculable condition would likewise be pivotal in showcasing the true effectiveness of cloning in MCEv1. Preliminary investigations into suitable conditions have already occurred. A natural starting point would be to follow the exact condition as in MCEv2. However, the computational cost would be too extreme to clone the entire wavefunction when a single basis function requires, it remains to be seen if there is an optimal fraction of straddled basis functions in which cloning the wavefunction would be both beneficial to the propagation and cost effective. With an ideal condition, cloning would be called very rarely, or even never in cases that MCEv1 has already been shown to provide fully converged accurate results. Further investigations into the behaviour of cross-terms can provide insight into the optimal cloning regions for each subset of the spin boson behaviour as cloning at a later stage of the propagation will save computational time if producing the same final result.

Chapter 3

Future work

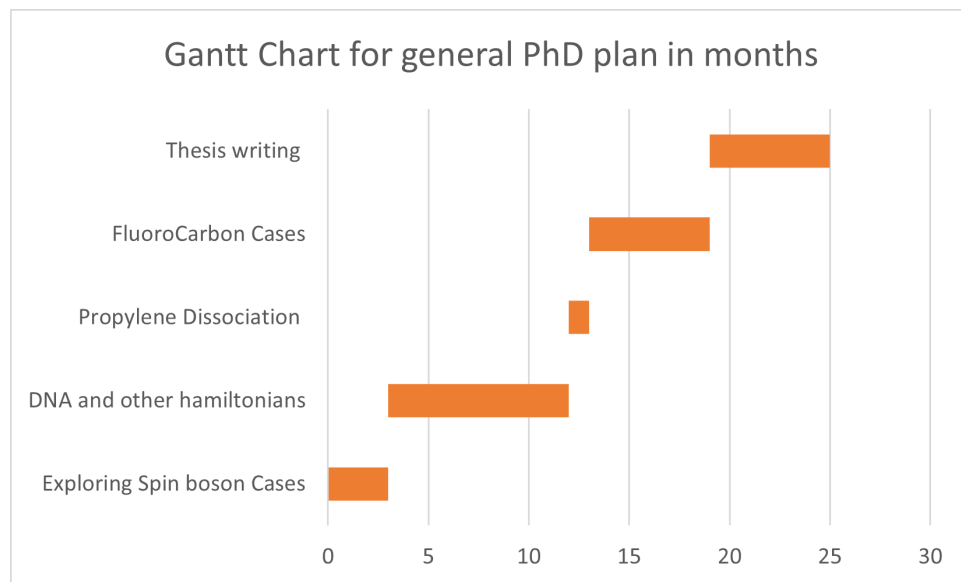
In order to fully test the effectiveness of cloning with cross-terms it is important to fully explore the multiple regimes of the spin boson model. To this aim, the method will be applied to the spaces of the spin boson model that were deemed difficult for other methods, as covered at the end of chapter 1. Firstly, cloning with cross-terms will be used to converge the rest of the cases specified in the zero temperature MCTDH paper. The method will also be applied to other areas that MCTDH has been applied to, such as difficult cases with a Debye spectral density.

If the method proves to be an effective way to produce converged results, the next step is to progress from the model cases to real practical Hamiltonians. MCEv1 has potential to be a method that scales efficiently enough to be capable of handling systems with large degrees of freedom, particularly in the cases of ultra-fast photo dynamics. This advantage might be capable of allowing MCE to be applied to cases that are usually tackled with density functional theory (DFT), such as work by former group member Dr James Green(118-120).

Another area that can be investigated by molecular dynamics is that of plasma chemistry. Plasma contributes to several vital processes involved in the etching of semiconductors. The plasma required in the production of these semiconductors is produced from primarily fluorocarbons, and the most popular industrial fluorocarbons often have a high global warming potential. This has led to several starting reagents being banned in an attempt to lower the contribution to climate change and a prediction that several more will be banned in the future. However, when these molecules are excited, the relaxation process often only involves the first triplet state and dissociation can occur on timescales that can be simulated by molecular dynamics

methods at sufficiently high temperatures. Research is currently ongoing in our research group to investigate the dissociation after excitation via electron impact, the process used to generate plasma. If results can be simulated to match existing experimental data(120,121), simulations of other molecules can provide industry with molecules that are efficient and cheap to source while also not causing adverse effects to the environment.

The introduction to this project would also be beneficial to the understanding of MCE methods, as it is a form of ab initio molecular dynamics. The research group has already developed an interface between molecular dynamic code and an electronic structure package, QChem. This introduction will provide insight and familiarity to any such ab initio method as the interaction between any nuclear dynamics code and an electronic structure package will be very similar providing useful experience for future projects. The project will begin with studying a test case molecule, propylene. Propylene is a sufficiently small and simple molecule that running trajectories and calculation the electronic structure will be quick enough to allow development of understanding of the code and project in general, due to results of ethane having been previously calculated within the group. These prior results can serve as a placement to ensure proper setup as well as reasonable expectations for computational times as well as the quantitative results can be used to establish a trend and extend understanding of the dissociation of alkenes.



Chapter 4

References

1. Shalashilin, D.V. Multiconfigurational Ehrenfest approach to quantum coherent dynamics in large molecular systems. *Faraday Discussions.* 2011, 153, pp.105-116.
2. Shalashilin, D.V. and Child, M.S. Basis set sampling in the method of coupled coherent states: Coherent state swarms, trains, and pancakes. *Journal of Chemical Physics.* 2008, 128(5).
3. Secrest, D. and Johnson, R.B. Exact Quantum-Mechanical calculation pf a collinear collision of a particle with a harmonic oscillator. *Journal of Chemical Physics.* 1966, 45(12), pp.4556-.
4. Miller, W.H. CLASSICAL S-MATRIX - Numerical application to inelastic collisions. *Journal of Chemical Physics.* 1970, 53(9), pp.3578-.
5. Miller, W.H. The classical S-matrix: A more detailed study of classically forbidden transitions in inelastic collisions. *Chemical Physics Letters.* 1970, 7(4), pp.431-435.
6. Miller, W.H. The semiclassical initial value representation: A potentially practical way for adding quantum effects to classical molecular dynamics simulations. *Journal of Physical Chemistry A.* 2001, 105(13), pp.2942-2955.
7. Thoss, M. and Wang, H.B. Semiclassical description of molecular dynamics based on initial-value representation methods. *Annual Review of Physical Chemistry.* 2004, 55, pp.299-332.
8. Lago, N.F. and Lagana, A. A comparison of semiclassical IVR and exact quantum collinear atom diatom transition probabilities for mixed reactive and non reactive regimes. In: 24th International Symposium on Rarefied Gas Dynamics (RGD24), Jul 10-16, Monopoli, ITALY.

2004, pp.920-925.

9. Lago, N.F. and Lagana, A. A semiclassical initial value representation approach to N+N-2 rate coefficient. In: International Conference on Computational Methods in Science and Engineering, Oct 27-Nov 01, Chania, GREECE. 2006, pp.297-300.
10. Wang, H.B., Thoss, M., Sorge, K.L., Gelabert, R., Gimenez, X. and Miller, W.H. Semiclassical description of quantum coherence effects and their quenching: A forward-backward initial value representation study. *Journal of Chemical Physics*. 2001, 114(6), pp.2562-2571.
11. Ceotto, M., Dell'Angelo, D. and Tantardini, G.F. Multiple coherent states semiclassical initial value representation spectra calculations of lateral interactions for CO on Cu(100). *Journal of Chemical Physics*. 2010, 133(5).
12. Kaledin, A.L. and Miller, W.H. Time averaging the semiclassical initial value representation for the calculation of vibrational energy levels. II. Application to H₂CO, NH₃, CH₄, CH₂D₂. *Journal of Chemical Physics*. 2003, 119(6), pp.3078-3084.
13. Elran, Y. and Kay, K.G. Semiclassical IVR treatment of reactive collisions. *Journal of Chemical Physics*. 2002, 116(24), pp.10577-10588.
14. Campolieti, G. and Brumer, P. Semiclassical initial value theory for dissociation dynamics. *Journal of Chemical Physics*. 1997, 107(3), pp.791-803.
15. Sun, X. and Miller, W.H. Mixed semiclassical-classical approaches to the dynamics of complex molecular systems. *Journal of Chemical Physics*. 1997, 106(3), pp.916-927.
16. Sun, X., Wang, H.B. and Miller, W.H. Semiclassical theory of electronically nonadiabatic dynamics: Results of a linearized approximation to the initial value representation. *Journal of Chemical Physics*. 1998, 109(17), pp.7064-7074.
17. Naseri, N.K., Sundararajan, E.A., Ayob, M. and Jula, A. Smart Root Search (SRS): A Novel Nature-Inspired Search Algorithm. *Symmetry-Basel*. 2020, 12(12).
18. Keshavamurthy, S. and Miller, W.H. SEMICLASSICAL CORRECTION FOR QUANTUM-MECHANICAL SCATTERING. *Chemical Physics Letters*. 1994, 218(3), pp.189-194.
19. Balzer, B., Dilthey, S., Stock, G. and Thoss, M. Quasiclassical and semiclassical wave-packet dynamics in periodic potentials. *Journal of Chemical Physics*. 2003, 119(12), pp.5795-5804.

20. Grossmann, F. Semiclassical real-time tunneling by multiple spawning of classical trajectories. *Physical Review Letters*. 2000, 85(5), pp.903-907.
21. Cohen, G., Gull, E., Reichman, D.R. and Millis, A.J. Taming the Dynamical Sign Problem in Real-Time Evolution of Quantum Many-Body Problems. *Physical Review Letters*. 2015, 115(26).
22. Kay, K.G. Semiclassical tunneling in the initial value representation. *Journal of Chemical Physics*. 1997, 107(7), pp.2313-2328.
23. Malpathak, S. and Ananth, N. Non-linear correlation functions and zero-point energy flow in mixed quantum-classical semiclassical dynamics. *Journal of Chemical Physics*. 2023, 158(10).
24. Malpathak, S., Church, M.S. and Ananth, N. A Semiclassical Framework for Mixed Quantum Classical Dynamics. *Journal of Physical Chemistry A*. 2022, 126(37), pp.6359-6375.
25. Ray, S., Ostmann, P., Simon, L., Grossmann, F. and Strunz, W.T. Dynamics of interacting bosons using the Herman–Kluk semiclassical initial value representation. *Journal of Physics A: Mathematical and Theoretical*. 2016, 49(16), p.165303.
26. Kay, K.G. Semiclassical initial value treatments of atoms and molecules. *Annual Review of Physical Chemistry*. 2005, 56, pp.255-+.
27. Batista, V.S., Zanni, M.T., Greenblatt, B.J., Neumark, D.M. and Miller, W.H. Femtosecond photoelectron spectroscopy of the I₂(-) anion: A semiclassical molecular dynamics simulation method. *Journal of Chemical Physics*. 1999, 110(8), pp.3736-3747.
28. Wang, H.B., Sun, X. and Miller, W.H. Semiclassical approximations for the calculation of thermal rate constants for chemical reactions in complex molecular systems. *Journal of Chemical Physics*. 1998, 108(23), pp.9726-9736.
29. Gelabert, R., Giménez, X., Thoss, M., Wang, H. and Miller, W.H. A Log-Derivative Formulation of the Prefactor for the Semiclassical Herman-Kluk Propagator. *The Journal of Physical Chemistry A*. 2000, 104(45), pp.10321-10327.
30. Sun, X. and Miller, W.H. Semiclassical initial value representation for rotational degrees of freedom: The tunneling dynamics of HCl dimer. *Journal of Chemical Physics*. 1998, 108(21), pp.8870-8877.

31. Skinner, D.E. and Miller, W.H. Application of the semiclassical initial value representation and its linearized approximation to inelastic scattering. *Chemical Physics Letters.* 1999, 300(1-2), pp.20-26.
32. Liu, J. Recent Advances in the Linearized Semiclassical Initial Value Representation/Classical Wigner Model for the Thermal Correlation Function. *International Journal of Quantum Chemistry.* 2015, 115(11), pp.657-670.
33. Miller, W.H. Generalization of the linearized approximation to the semiclassical initial value representation for reactive flux correlation functions. *Journal of Physical Chemistry A.* 1999, 103(47), pp.9384-9387.
34. Heller, E.J. Time-Dependent approach to semiclassical dynamics. *Journal of Chemical Physics.* 1975, 62(4), pp.1544-1555.
35. Buch, V. Calculation of infrared absorption spectra using Gaussian variational wave packets. *Journal of Chemical Physics.* 2004, 121(14), pp.6961-6966.
36. Buch, V. Exploration of multidimensional variational Gaussian wave packets as a simulation tool. *Journal of Chemical Physics.* 2002, 117(10), pp.4738-4750.
37. Vaníček, J. and Begušić, T. Ab Initio Semiclassical Evaluation of vibrationally Resolved Electronic Spectra With Thawed Gaussians. In: *Molecular Spectroscopy and Quantum Dynamics.* Elsevier, 2021, pp.199-229.
38. Begusic, T., Patoz, A., Sulc, M. and Vanicek, J. On-the-fly ab initio three thawed Gaussians approximation: A semiclassical approach to Herzberg-Teller spectra. *Chemical Physics.* 2018, 515, pp.152-163.
39. Heller, E.J. FROZEN GAUSSIANS - A very simple semi-classical approximation. *Journal of Chemical Physics.* 1981, 75(6), pp.2923-2931.
40. De Leon, N. and Heller, E.J. Semiclassical quantization and extraction of eigenfunctions using arbitrary trajectories. *The Journal of Chemical Physics.* 1983, 78(6), pp.4005-4017.
41. Herman, M.F. Time reversal and unitarity in the frozen Gaussian approximation for semiclassical scattering. *The Journal of Chemical Physics.* 1986, 85(4), pp.2069-2076.
42. Sepulveda, M.A. Comment on the Breakdown of Van Vleck's Propagator and Its Implications. *Journal of Chemical Physics.* 1987, 86(10), pp.5370-5372.

- tions for the Energy Domain Green's Function. Progress of Theoretical Physics Supplement. 1994, (116), pp.277-282.
43. Chai, L.H., Lorin, E. and Yang, X. FROZEN GAUSSIAN APPROXIMATION FOR THE DIRAC EQUATION IN SEMICLASSICAL REGIME. Siam Journal on Numerical Analysis. 2019, 57(5), pp.2383-2412.
44. Delgadillo, R., Yang, X. and Zhang, J.W. Frozen Gaussian Approximation-Based Artificial Boundary Conditions for One-Dimensional Nonlinear Schrodinger Equation in the Semiclassical Regime. Journal of Scientific Computing. 2018, 75(3), pp.1701-1720.
45. Delgadillo, R., Lu, J.F. and Yang, X. Gauge-Invariant Frozen Gaussian Approximation Method for the Schrodinger Equation with Periodic Potentials. Siam Journal on Scientific Computing. 2016, 38(4), pp.A2440-A2463.
46. Tatchen, J., Pollak, E., Tao, G.H. and Miller, W.H. Renormalization of the frozen Gaussian approximation to the quantum propagator. Journal of Chemical Physics. 2011, 134(13).
47. Kondorskiy, A. and Nakamura, H. Semiclassical frozen Gaussian propagation method for electronically nonadiabatic chemical dynamics: Moller operator formulation and incorporation of the Zhu-Nakamura theory. Journal of Theoretical Computational Chemistry. 2005, 4(1), pp.89-102.
48. Gelman, D. and Schwartz, S.D. Tunneling dynamics with a mixed quantum-classical method: Quantum corrected propagator combined with frozen Gaussian wave packets. Journal of Chemical Physics. 2008, 129(2).
49. Shalashilin, D.V. and Child, M.S. Time dependent quantum propagation in phase space. Journal of Chemical Physics. 2000, 113(22), pp.10028-10036.
50. Ronto, M. and Shalashilin, D.V. Numerical Implementation and Test of the Modified Variational Multiconfigurational Gaussian Method for High-Dimensional Quantum Dynamics. Journal of Physical Chemistry A. 2013, 117(32), pp.6948-6959.
51. Child, M.S. and Shalashilin, D.V. Locally coupled coherent states and Herman-Kluk dynamics. Journal of Chemical Physics. 2003, 118(5), pp.2061-2071.
52. Shalashilin, D.V. and Child, M.S. Nine-dimensional quantum molecular dynamics simulation of intramolecular vibrational energy redistribution in the CHD₃ molecule with the help of

- coupled coherent states. *Journal of Chemical Physics.* 2003, 119(4), pp.1961-1969.
53. Shalashilin, D. and Child, M. Quantum propagation on trajectory guided random grids of coupled coherent states. *Abstracts of Papers of the American Chemical Society.* 2004, 227, pp.U279-U279.
54. Shalashilin, D.V., Child, M.S. and Clary, D.C. Quantum initial value representation simulation of water trimer far infrared absorption spectrum. *Journal of Chemical Physics.* 2004, 120(12), pp.5608-5615.
55. Shalashilin, D.V. and Child, M.S. Real time quantum propagation on a Monte Carlo trajectory guided grids of coupled coherent states: 26D simulation of pyrazine absorption spectrum. *Journal of Chemical Physics.* 2004, 121(8), pp.3563-3568.
56. Shalashilin, D.V. Quantum mechanics with the basis set guided by Ehrenfest trajectories: Theory and application to spin-boson model. *Journal of Chemical Physics.* 2009, 130(24).
57. Wolf, P. Topical DNA repair enzymes: A novel approach to photoprotection. *Journal of Investigative Dermatology.* 2006, 126, pp.S19-S19.
58. Megna, M., Lembo, S., Balato, N. and Monfrecola, G. "Active" photoprotection: sunscreens with DNA repair enzymes. *Giornale Italiano Di Dermatologia E Venereologia.* 2017, 152(3), pp.302-307.
59. Rodrigues, N.D.N., Cole-Filipliak, N.C., Blodgett, K.N., Abeysekera, C., Zwier, T.S. and Stavros, V.G. Wavepacket insights into the photoprotection mechanism of the UV filter methyl anthranilate. *Nature Communications.* 2018, 9.
60. Mathies, R.A., Cruz, C.H.B., Pollard, W.T. and Shank, C.V. Direct Observation of the Femtosecond Excited-State cis-trans Isomerization in Bacteriorhodopsin. *Science.* 1988, 240(4853), pp.777-779.
61. Edholm, O. and Jahnig, F. MOLECULAR-DYNAMICS SIMULATIONS OF BACTERIORHODOPSIN. In: 25th Jerusalem Symp on Quantum Chemistry and Biochemistry, May 18-21, Jerusalem, Israel. 1992, pp.47-60.
62. Woolf, T.B. Molecular dynamics simulations of individual bacteriorhodopsin helices. *Biochemical Journal.* 1996, 70(2), pp.WAML8-WAML8.

63. Watanabe, M., Soosaar, K. and Chun, H.M. Multigranular molecular dynamics simulations of Bacteriorhodopsin. Abstracts of Papers of the American Chemical Society. 1998, 216, pp.U687-U687.
64. Hayashi, S., Tajkhorshid, E. and Schulten, K. Molecular Dynamics Simulation of Bacteriorhodopsin's Photoisomerization Using Ab Initio Forces for the Excited Chromophore. Biophysical Journal. 2003, 85(3), pp.1440-1449.
65. Wang, H.B. Basis set approach to the quantum dissipative dynamics: Application of the multiconfiguration time-dependent Hartree method to the spin-boson problem. Journal of Chemical Physics. 2000, 113(22), pp.9948-9956.
66. Wang, H.B. and Thoss, M. Multilayer formulation of the multiconfiguration time-dependent Hartree theory. Journal of Chemical Physics. 2003, 119(3), pp.1289-1299.
67. Shalashilin, D.V. Nonadiabatic dynamics with the help of multiconfigurational Ehrenfest method: Improved theory and fully quantum 24D simulation of pyrazine. Journal of Chemical Physics. 2010, 132(24).
68. Makhov, D.V., Glover, W.J., Martinez, T.J. and Shalashilin, D.V. Ab initio multiple cloning algorithm for quantum nonadiabatic molecular dynamics. Journal of Chemical Physics. 2014, 141(5).
69. Symonds, C., Kattirtzi, J.A. and Shalashilin, D.V. The effect of sampling techniques used in the multiconfigurational Ehrenfest method. Journal of Chemical Physics. 2018, 148(18).
70. Ben-Nun, M., Quenneville, J. and Martinez, T.J. Ab initio multiple spawning: Photochemistry from first principles quantum molecular dynamics. Journal of Physical Chemistry A. 2000, 104(22), pp.5161-5175.
71. Martinez, T.J. Insights for light-driven molecular devices from ab initio multiple spawning excited-state dynamics of organic and biological chromophores. Accounts of Chemical Research. 2006, 39(2), pp.119-126.
72. Curchod, B.F.E., Glover, W.J. and Martinez, T.J. SSAIMS-Stochastic-Selection Ab Initio Multiple Spawning for Efficient Nonadiabatic Molecular Dynamics. Journal of Physical Chemistry A. 2020, 124(30), pp.6133-6143.
73. Mignolet, B. and Curchod, B.F.E. A walk through the approximations of ab initio multiple

- spawning. *Journal of Chemical Physics.* 2018, 148(13).
74. Hack, M.D., Wensmann, A.M., Truhlar, D.G., Ben-Nun, M. and Martinez, T.J. Comparison of full multiple spawning, trajectory surface hopping, and converged quantum mechanics for electronically nonadiabatic dynamics. *Journal of Chemical Physics.* 2001, 115(3), pp.1172-1186.
75. Wensmann, A.M., Hack, M.D., Truhlar, D.G. and Martinez, T.J. Systematic test of the full multiple spawning method for photochemical dynamics. *Abstracts of Papers of the American Chemical Society.* 2001, 221, pp.U276-U276.
76. Ben-Nun, M. and Martinez, T.J. A multiple spawning approach to tunneling dynamics. *Journal of Chemical Physics.* 2000, 112(14), pp.6113-6121.
77. Green, J.A., Makhov, D.V., Cole-Filipliak, N.C., Symonds, C., Stavros, V.G. and Shalashilin, D.V. Ultrafast photodissociation dynamics of 2-ethylpyrrole: adding insight to experiment with ab initio multiple cloning. *Physical Chemistry Chemical Physics.* 2019, 21(7), pp.3832-3841.
78. Symonds, C.C., Makhov, D.V., Cole-Filipliak, N.C., Green, J.A., Stavros, V.G. and Shalashilin, D.V. Ultrafast photodissociation dynamics of pyrazole, imidazole and their deuterated derivatives using ab initio multiple cloning. *Physical Chemistry Chemical Physics.* 2019, 21(19), pp.9987-9995.
79. Makhov, D.V., Martinez, T.J. and Shalashilin, D.V. Toward fully quantum modelling of ultrafast photodissociation imaging experiments. Treating tunnelling in the ab initio multiple cloning approach. *Faraday Discussions.* 2016, 194, pp.81-94.
80. Song, H.J., Freixas, V.M., Fernandez-Alberti, S., White, A.J., Zhang, Y., Mukamel, S., Govind, N. and Tretiak, S. An Ab Initio Multiple Cloning Method for Non-Adiabatic Excited-State Molecular Dynamics in NWChem. *Journal of Chemical Theory and Computation.* 2021, 17(6), pp.3629-3643.
81. Makhov, D.V., Saita, K., Martinez, T.J. and Shalashilin, D.V. Ab initio multiple cloning simulations of pyrrole photodissociation: TKER spectra and velocity map imaging. *Physical Chemistry Chemical Physics.* 2015, 17(5), pp.3316-3325.
82. Makhov, D.V., Adeyemi, S., Cowperthwaite, M. and Shalashilin, D.V. Simulation of the dynamics of vibrationally mediated photodissociation for deuterated pyrrole. *Journal of Physics*

Communications. 2022, 6(2), p.025001.

83. Makhov, D.V. and Shalashilin, D.V. Simulation of the effect of vibrational pre-excitation on the dynamics of pyrrole photo-dissociation. *Journal of Chemical Physics*. 2021, 154(10).
84. Le Hur, K. Entanglement entropy, decoherence, and quantum phase transitions of a dissipative two-level system. *Annals of Physics*. 2008, 323(9), pp.2208-2240.
85. Kopp, A. and Le Hur, K. Universal and measurable entanglement entropy in the spin-boson model. *Physical Review Letters*. 2007, 98(22).
86. Leggett, A.J., Chakravarty, S., Dorsey, A.T., Fisher, M.P.A., Garg, A. and Zwerger, W. Dynamics of the dissipative two-state system. *Reviews of Modern Physics*. 1987, 59(1), pp.1-85.
87. Suarez, A. and Silbey, R. Properties of a macroscopic system as a thermal bath. *Journal of Chemical Physics*. 1991, 95(12), pp.9115-9121.
88. Weiss, U., Grabert, H. and Linkwitz, S. Influence of friction and temperature on coherent quantum tunneling. *Journal of Low Temperature Physics*. 1987, 68(3-4), pp.213-244.
89. Luck, A., Winterstetter, M., Weiss, U. and Mak, C.H. Quantum Monte Carlo simulations of driven spin-boson systems. *Physical Review E*. 1998, 58(5), pp.5565-5573.
90. Nan, G.J. and Li, Z.S. Stationary phase approximation of electron transfer rate constants for the spin-boson model with Debye spectral density. *Computational and Theoretical Chemistry*. 2011, 967(2-3), pp.226-230.
91. Thoss, M., Wang, H.B. and Miller, W.H. Self-consistent hybrid approach for complex systems: Application to the spin-boson model with Debye spectral density. *Journal of Chemical Physics*. 2001, 115(7), pp.2991-3005.
92. Wang, H.B., Song, X.Y., Chandler, D. and Miller, W.H. Semiclassical study of electronically nonadiabatic dynamics in the condensed-phase: Spin-boson problem with Debye spectral density. *Journal of Chemical Physics*. 1999, 110(10), pp.4828-4840.
93. Lambert, N., Ahmed, S., Cirio, M. and Nori, F. Modelling the ultra-strongly coupled spin-boson model with unphysical modes. *Nature Communications*. 2019, 10.
94. Toutounji, M.M. and Small, G.J. The underdamped Brownian oscillator model with Ohmic dissipation: Applicability to low-temperature optical spectra. *Journal of Chemical Physics*.

- 2002, 117(8), pp.3848-3855.
95. Manthe, U. The multi-configurational time-dependent Hartree approach revisited. *Journal of Chemical Physics*. 2015, 142(24).
96. Manthe, U. Wavepacket dynamics and the multi-configurational time-dependent Hartree approach. *Journal of Physics-Condensed Matter*. 2017, 29(25).
97. Meyer, H.D., Manthe, U. and Cederbaum, L.S. The multi-configurational time-dependent Hartree approach. *Chemical Physics Letters*. 1990, 165(1), pp.73-78.
98. Ben-Nun, M. and Martinez, T.J. A continuous spawning method for nonadiabatic dynamics and validation for the zero-temperature spin-boson problem. *Israel Journal of Chemistry*. 2007, 47(1), pp.75-88.
99. Dekker, H. Dynamics of the dissipative 2-state system - the noninteracting blip approximation. *Physica A*. 1987, 141(2-3), pp.570-574.
100. Dekker, H. Noninteracting-blip approximation for a two-level system coupled to a heat bath. *Physical Review A*. 1987, 35(3), pp.1436-1437.
101. Giraldi, F. and Petruccione, F. Arbitrarily Slow Relaxations in a Spin-Boson Model Under the Noninteracting-Blip Approximation. *International Journal of Quantum Information*. 2012, 10(8).
102. Wang, H.B. and Thoss, M. From coherent motion to localization: dynamics of the spin-boson model at zero temperature. *New Journal of Physics*. 2008, 10.
103. Tanimura, Y. and Kubo, R. Time Evolution of a Quantum System in Contact with a Nearly Gaussian-Markoffian Noise Bath. *Journal of the Physical Society of Japan*. 1989, 58(1), pp.101-114.
104. Tanimura, Y. Numerically "exact" approach to open quantum dynamics: The hierarchical equations of motion (HEOM). *Journal of Chemical Physics*. 2020, 153(2).
105. Ikeda, T. and Scholes, G.D. Generalization of the hierarchical equations of motion theory for efficient calculations with arbitrary correlation functions. *Journal of Chemical Physics*. 2020, 152(20).
106. Kato, A. and Tanimura, Y. Quantum heat current under non-perturbative and non-

- Markovian conditions: Applications to heat machines. *Journal of Chemical Physics.* 2016, 145(22).
107. Chen, L.P., Zheng, R.H., Shi, Q. and Yan, Y.J. Optical line shapes of molecular aggregates: Hierarchical equations of motion method. *Journal of Chemical Physics.* 2009, 131(9).
108. Chen, L.P., Zheng, R.H., Shi, Q. and Yan, Y.J. Two-dimensional electronic spectra from the hierarchical equations of motion method: Application to model dimers. *Journal of Chemical Physics.* 2010, 132(2).
109. Ishizaki, A. and Fleming, G.R. Quantum Coherence in Photosynthetic Light Harvesting. *Annual Review of Condensed Matter Physics,* Vol 3. 2012, 3, pp.333-361.
110. Chen, L.P., Yan, Y.Y., Gelin, M.F. and Lue, Z.G. Dynamics of the spin-boson model: The effect of bath initial conditions. *Journal of Chemical Physics.* 2023, 158(10).
111. Duan, C.R., Wang, Q.L., Tang, Z.F. and Wu, J.L. The study of an extended hierarchy equation of motion in the spin-boson model: The cutoff function of the sub-Ohmic spectral density. *Journal of Chemical Physics.* 2017, 147(16).
112. Anders, F.B., Bulla, R. and Vojta, M. Equilibrium and nonequilibrium dynamics of the sub-Ohmic spin-boson model. *Physical Review Letters.* 2007, 98(21).
113. Kirchner, S., Ingersent, K. and Si, Q.M. Quantum criticality of the sub-Ohmic spin-boson model. *Physical Review B.* 2012, 85(7).
114. Gan, C.J. and Zheng, H. Non-Markovian dynamics of a dissipative two-level system: Nonzero bias and sub-Ohmic bath. *Physical Review E.* 2009, 80(4).
115. Kehrein, S.K. and Mielke, A. On the spin-boson model with a sub-ohmic bath. *Physics Letters A.* 1996, 219(5-6), pp.313-318.
116. Yao, Y. and Zhao, Y. A variational surface hopping algorithm for the sub-Ohmic spin-boson model. *Journal of Chemical Physics.* 2013, 139(1).
117. Wang, H.B. and Thoss, M. From coherent motion to localization: II. Dynamics of the spin-boson model with sub-Ohmic spectral density at zero temperature. *Chemical Physics.* 2010, 370(1-3), pp.78-86.
118. Green, J.A. and Imrota, R. Vibrations of the guanine-cytosine pair in chloroform: an

anharmonic computational study. *Physical Chemistry Chemical Physics.* 2020, 22(10), pp.5509-5522.

119. Green, J.A., Jouybari, M.Y., Aranda, D., Improta, R. and Santoro, F. Nonadiabatic Absorption Spectra and Ultrafast Dynamics of DNA and RNA Photoexcited Nucleobases. *Molecules.* 2021, 26(6).

120. Jouybari, M.Y., Green, J.A., Improta, R. and Santoro, F. The Ultrafast Quantum Dynamics of Photoexcited Adenine-Thymine Basepair Investigated with a Fragment-based Diabatization and a Linear Vibronic Coupling Model. *Journal of Physical Chemistry A.* 2021, 125(40), pp.8912-8924.

120. Kim, Y., Kim, S., Kang, H., You, S., Kim, C. and Chae, H. Low Global Warming C₄H₃F₇O Isomers for Plasma Etching of SiO₂ and Si₃N₄ Films. *Acs Sustainable Chemistry and Engineering.* 2022, 10(32), pp.10537-10546.

121. Kim, Y., Kang, H., Kim, C. and Chae, H. Plasma Atomic Layer Etching of SiO₂ and Si₃N₄ with Low Global Warming C₄H₃F₇O Isomers. *Acs Sustainable Chemistry and Engineering.* 2023, 11(16), pp.6136-6142.